Check for updates

NANO · MICRO small
www.small-journal.com

Synergistic Interactions Between Single Atoms and Clusters/Nanoparticles on Nitrogen-Doped Carbon Supports for Electrocatalysis: A Critical Review

Thanh Duc Le, Van Hien Hoa, Khoa Dang Tran, Do Hwan Kim, Vandung Dao, In-Hwan Lee, Dong-Seog Kim, Tuong Van Tran, and Yeon-Tae Yu**

Since the discovery of single-atom catalysts (SACs) in 2011, research has primarily focused on achieving atomic dispersion, which can lead to their remarkable catalytic activity, selectivity, and atom utilization. In parallel, nanoparticles (NPs)-based catalysts have a long-standing history and a proven track record in electrocatalysis. Integration of single atoms (SAs) and NPs within a single catalytic framework has recently emerged as a promising strategy to enhance electrocatalytic performance beyond what each component can achieve on its own. Therefore, understanding these synergistic interactions is crucial for improving the activity, selectivity, and long-term stability of hybrid catalysts. Despite this potential, systematic investigations on these hybrid catalyst systems are relatively limited and present significant challenges. This review provides a comprehensive overview of the structural classifications, mechanistic insights, and recent advances in electrocatalytic applications of SA-NP hybrid systems. We further highlight synthetic strategies for nitrogen-doped carbon materials as supports that co-stabilize SAs and NPs, and critically discuss key challenges and future perspectives for the rational design and application of these advanced electrocatalysts are critically discussed.

1. Introduction

The constrained availability of primary energy sources, including fossil fuels, together with increasing global energy demands driven by population growth and environmental concerns, presents significant challenges to human health, energy security, and ecological sustainability.[1–3] A promising strategy for addressing these challenges is the production, storage, and utilization of clean and renewable sources.[4–6] In the coming decades, substantial progress and broad commercialization of electrochemical energy conversion and storage technologies are anticipated, particularly in water electrolyzes, metal-air batteries, and fuel cells.[7,8] In this regard, at the core of these technologies, the electrocatalytic reactions, such as oxygen reduction reaction (ORR), hydrogen evolution reaction (HER), oxygen evolution reaction (OER), carbon dioxide reduction (CO_2RR), nitrogen reduction reaction (NRR), need to be emphasized.[9,10]

Traditionally, platinum group metals (PGM) catalysts have been regarded as the best catalysts for such electrochemical reactions.[11,12] However, their high cost, poor durability and low availability have severely restricted their widespread deployment in large-scale energy applications.[13,14] To reduce the reliance on PGMs, two main strategies are being pursued: 1) the development

T. D. Le
Center for Advanced Chemistry
Institute of Research and Development
Duy Tan University
Da Nang 550000, Vietnam
E-mail: leducthanh3@duytan.edu.vn

T. D. Le
Faculty of Natural Sciences
Duy Tan University
Da Nang 550000, Vietnam

V. H. Hoa
Department of Nano Convergence Engineering
Jeonbuk National University
Jeonju, Jeonbuk 54896, Republic of Korea

K. D. Tran
Faculty of Information Technology
University of Transport Technology
Hanoi 100000, Vietnam

D. H. Kim
Division of Science Education and Institute for Fusion Science
Graduate School of the Department of Energy Storage/Conversion Engineering
Jeonbuk National University
Jeonju, Jeonbuk 54896, Republic of Korea

V. Dao, I.-H. Lee
Department of Materials Science and Engineering
Korea University
Seoul 02841, Republic of Korea

D.-S. Kim, T. V. Tran, Y.-T. Yu
Division of Advanced Materials Engineering
Research Center for Advanced Materials Development
Jeonbuk National University
Jeonju 54896, Republic of Korea
E-mail: yeontae@jbnu.ac.kr

The ORCID identification number(s) for the author(s) of this article can be found under https://doi.org/10.1002/smll.202512014

DOI: 10.1002/smll.202512014

 © 2025 Wiley-VCH GmbH

of non-noble metal catalysts and 2) the enhancement of Pt utilization efficiency. Considerable efforts have focused on replacing PGMs with non-noble metals for electrocatalysis applications.[15–20] Among these, M-N-C catalysts (where M represents transition metals) have demonstrated the highest catalytic performance and are the most extensively studied.[21] These materials are typically synthesized via high-temperature pyrolysis of nitrogen- and metal-containing carbon precursors.[22,23] In addition to their cost-effectiveness, M-N-C catalysts usually exhibit greater tolerance to fuel poisoning (e.g., methanol and ethanol) compared to commercial PGM-based catalysts.[24–26] Nevertheless, there is a significant performance gap between non-noble metal catalysts and commercial PGM under acidic conditions.[27] Reducing PGM loading can be achieved by employing highly dispersed PGM nanoparticles onto support, through alloying with transition metals, or through the development of novel PGM structures.[28–32] Yet, non-PGM electrocatalysts continue to face challenges due to the low durability of transition metals and the persistent deactivation.

Another promising route to decrease PGM loading is to maximize atomic utilization. The emergence of single-atom catalysts (SACs) in 2011 marked a significant breakthrough in this direction,[33] and it quickly became a new research era in the field of catalysis. Owing to their maximized atomic efficiency,[34] SACs have attracted extensive attention across diverse fields, including catalysis,[35–40] sensors,[41,42] biomedicine[43] and others. Importantly, the performance and selectivity of the SACs can be precisely tuned by manipulating the coordination environment around the individual metal atoms. In particular, N-doped carbon has proven to be an effective support material. It not only stabilizes the single metal atom site but also modulates their local electronic structure, thereby enhancing electron transfer and boosting activity in reactions such as the ORR, OER, HER, etc.[44–48]

Despite significant advances, current efforts largely focus on developing either nanoscale or atomic-scale catalysts independently, while the potential synergistic interactions between single atoms (SAs) and nanoparticles (NPs) in hybrid systems remain underexplored. In this review, we summarize recent progress in SA-NP hybrid electrocatalysts, highlighting representative examples, synthetic strategies, and the fundamental electronic and chemical interactions that govern their performance. We also discuss advances in nitrogen-doped carbon materials as supports for stabilizing both SAs and NPs, with particular emphasis on morphology control, nitrogen functionalization, and structural engineering. The aim of this review is to provide a research overview for a wide range of researchers and to encourage deeper interest and engagement in related research areas. Finally, we present challenges, opportunities, and future outlooks for the rational design and application of SA-NP hybrid catalysts in electrochemical energy conversion.

2. Synergistic Effects between SA and NPs

The hybridization between SAs and NPs is a cutting-edge approach in heterogeneous catalysis that combines the unique strengths of both catalytic entities to achieve synergistic performance that neither could accomplish individually.[49,50] The synergistic interactions between SAs and NPs have been shown to significantly enhance catalytic performance, offering a practical and attractive approach for advanced catalyst design.[51] When both SAs and NPs are anchored on the same support, their spatial proximity allows for various interactions, which must be carefully considered to fully exploit their cooperative behavior. Depending on factors such as the reaction type, metal loading, spatial arrangement, and the physicochemical nature of the support, the synergistic interactions between SAs and NPs can generally be categorized into three main types:

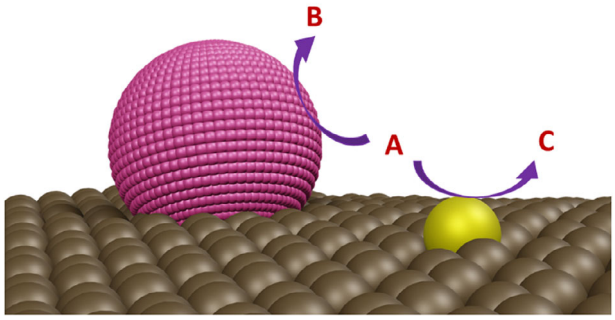


Figure 1. Parallel synergistic effect as a bifunctional catalyst with supported SA-NPs.

1) parallel synergistic effect, where both species independently contribute to the catalytic process[52,53] (typically, such as HER vs OER, OER vs ORR, etc.);
2) electronic interaction synergistic effect, where charge transfer or electronic modulation occurs between SAs and NPs,[54] altering their catalytic properties (including ORR, HER, OER, CO_2-to-CO conversion, etc.);
3) tandem synergistic effect, where SAs and NPs promote sequential reaction steps, each serving a distinct role in the cascade reaction pathway[55,56] (typically, an elementary step in CO_2RR, HER, ORR, etc.).

Based on this framework, the latest advances and representative studies are summarized and discussed in this section.

2.1. Parallel Synergistic Effect

Parallel synergistic effect refers to a catalytic mechanism in which two distinct types of active sites simultaneously and independently catalyze separate reaction components within the same system, each active site operates on its own substrate without direct interaction or electron transfer with the other (as shown in **Figure 1**). In multi-step or complex catalytic reaction, to achieve the optimal activity performance, the catalysts usually require the contribution of spatially defined multiple active sites with different catalytic properties.[57] The unique architecture of SA-NP hybrid catalysts is particularly well-suited for this purpose, as it enables each component to engage in distinct elementary steps along a reaction pathway, thereby enhancing overall reaction efficiency and selectivity. Furthermore, the coexistence of multiple active sites in such systems not only enhances the performance of individual reactions but also imparts bifunctional capabilities. This enables the catalyst to independently facilitate different reactions, broadening its applicability to multifunctional or tandem catalytic processes.[58]

© 2025 Wiley-VCH GmbH

16136829, 2026, 6, Downloaded from https://onlinelibrary.wiley.com/doi/10.1002/smll.202512014 by Jeonbuk National University, Wiley Online Library on [18/10/2026]. See the Terms and Conditions (https://onlinelibrary.wiley.com/terms-and-conditions) on Wiley Online Library for rules of use; OA articles are governed by the applicable Creative Commons License

For example, Hao et al. developed a bifunctional oxygen electrocatalyst composed of single Fe atoms coupled with $NiFe_2O_4$ NPs via π–π interaction (**Figure 2**) for zinc-air battery(ZAB) application.[59] High-angle annular dark-field scanning transmission electron microscopy (HADDF-STEM) analysis confirmed the coexistence of atomically dispersed Fe-N_4 sites and $NiFe_2O_4$ NPs within the catalyst matrix (Figure 2a). The FePc||$NiFe_2O_4$/G catalyst exhibited good bifunctional electrocatalytic performance, delivering a half-wave potential ($E_{1/2}$) of 0.852 V for the ORR (Figure 2b), which is slightly more positive than that of the benchmark Pt/C catalyst (0.843 V). For the OER in Figure 2c, the catalyst achieved a lower overpotential of 1.572 V at a current density of 10 mA cm^{-2}, outperforming the commercial Ir/C catalyst (1.615 V). To demonstrate the parallel synergistic effect between Fe-N_4 single sites and $NiFe_2O_4$ NPs, control experiments were conducted using samples containing only Fe single sites (FePc/G), only $NiFe_2O_4$ NPs ($NiFe_2O_4$/G), and the SA-NP hybrid electrocatalyst (FePc||$NiFe_2O_4$/G). These were tested for both ORR and OER performance. The ORR activity of FePc/G was nearly identical to that of FePc||$NiFe_2O_4$/G, indicating that the high ORR activity originates from Fe-N_4 sites (Figure 2d). Conversely, the OER activity of $NiFe_2O_4$/G was comparable to that of FePc||$NiFe_2O_4$/G (Figure 2e), demonstrating that the main OER active sites derive from $NiFe_2O_4$ NPs. These experimental results confirm the parallel synergistic effect of FePc||$NiFe_2O_4$/G catalyst, whereas single-atom Fe-N_4 moieties serve the primary active centers for ORR, and the nanosized $NiFeO_4$ species promote the OER activity (Figure 2f). In a recent report, Jing et al.[60] demonstrated the parallel synergistic effect between Fe SA and Co NPs through both experiments and density functional theory (DFT) calculation. The 3D porous Fe_{SA}-Co_{NP}@NC electrocatalyst consisting of tiny metallic Co NPs (Figure 2g) and Fe-N_4C SA (Figure 2h) supported on N-doped carbon was synthesized by pyrolysis combined with the metal macrocyclic compounds coupling method. The potential difference (ΔE) between $E_{j=10}$ of OER and $E_{1/2}$ of ORR reveals that the value of Fe_{SA}-Co_{NP}@NC-2 is 0.63 V (Figure 2i), which is obviously better than the ΔE (0.77 V) of Pt/C + RuO_2, indicating remarkable bifunctional activity for oxygen electrocatalysis. The authors also conducted poisoning experiments using thiocyanate (SCN^-) and ethylenediaminetetraacetic acid ($EDTA^{2-}$) to identify the primary active sites of the catalyst. The results revealed that Fe SAs predominantly catalyze the ORR, while Co NPs are mainly responsible for the OER. To further validate the parallel synergistic effect between Fe SAs and Co NPs, DFT calculations were carried out. The proposed mechanism for ORR and OER, along with the optimized $^*OH$, $^*O$, and $^*OOH$ intermediates on the FeN_4-Co NP model, is illustrated in Figure 2j–l. For ORR, the rate-determining step (RDS) on the Fe site is OH desorption, with a limiting potential of 0.74 V, significantly lower than that on the adjacent Co NP (1.89 V). In contrast, for OER, the RDS on the Co NP involves OOH deprotonation and O_2 formation, with a reduced limiting potential of 1.07 V. Besides, Yi-Yin and coworkers[61] embedded FeNi nanoparticles into the carbon wall via a carbothermic reaction to enhance OER activity, while isolated Fe atoms from iron phthalocyanine were anchored onto the wall through π–π interactions to catalyze the ORR. A similar bifunctional effect was observed in the co-reduction of CO_2 and H_2O using a Ni_{SA}+Ni_{NPs}/N-C catalyst. Zhu and his colleagues demonstrated that atomically dispersed Ni_{SA} show high activity toward CO_2 reduction and Ni_{NPs} catalyses the HER. Notably, by adjusting the atomic ratio of Ni_{SA} to Ni_{NPs} via an acid etching method, the catalyst can electrochemically produce syngas with a CO/H_2 ratio tunable from 1:9 to 19:1.[62] The author also investigated the dependence of Ni_{SA}+Ni_{NPs}/N-C ratio on various acid etching times and the corresponding CO/H_2 syngas ratios at −0.65 V vs RHE.

2.2. Electronic Interaction Synergistic Effect

The electronic interaction synergistic effect in catalysis refers to the phenomenon where adjacent metal species, such as SAs and NPs, interact through electronic communication (**Figure 3**).[63,64] This interaction involves charge transfer, orbital hybridization, or modification of the electronic structure between the two catalytic sites, which alters their individual catalytic properties and enhances overall catalytic performance. Fundamentally, most of the SA have narrow d-bands, while NPs display broad d-bands, so it is often difficult for SA or NPs catalysts to simultaneously achieve low activation barriers for reactions and weak binding between/in complex reactions with multi-intermediate coordinates.[59,62] A popular strategy to improve catalytic performance is to precisely regulate electron transfer to optimize the electronic structure of the active site. Many reports have confirmed that the co-existence of SAs and NPs can indeed effectively tailor the charge distribution state of the catalyst system, which can provide a pathway to explore the catalytic mechanism at the sub-nanometer scale.[65] The electronic interaction synergy has been demonstrated to enhance the adsorption/desorption and transfer behavior of reactions, intermediates, and products through electron transfer effects between different active sites.[66] The electronic interaction effect, particularly modulation of the d-band center, has been widely recognized as a critical factor influencing electrocatalytic activity in reactions such as ORR, HER, OER, and overall water splitting. The d-band center serves as the primary electronic descriptor controlling catalytic activity by determining the binding strength of reaction intermediates on the catalyst surface.[67,68] According to the d-band center theory, when the metal d-band center shifts closer to the Fermi level, stronger orbital overlap between metal d-orbitals and adsorbate p-orbitals strengthens intermediate binding; conversely, away from the Fermi level weakens binding.[69,70]

Wei et al.,[71] demonstrated that in situ construction of Pt_{NP}-Mn_{SA} pairs on a carbon support can significantly enhance ORR activity (**Figure 4a**). HAADF-STEM imaging revealed Pt_{NP} surrounded by densely distributed Mn SAs, distinguishable by their weaker Z-contrast (Figure 4b). Elemental line profiles confirmed the spatial correlation of Pt, Mn, and N species, indicating the formation of adjacent Mn_{SA} during annealing (Figure 4c). EXAFS analysis further identified a new peak at ≈2.7 Å, attributed to a Mn-Pt coordination shell, confirming the establishment of Mn—Pt bonds (Figure 4d). These results suggest the presence of well-defined Pt_{NP}-Mn_{SA} pairs within the catalyst. The Mn K-edge XANES spectra showed that both Mn_{SA}/C and Pt_{NP}-Mn_{SA}/C exhibited Mn valence states close to MnO (+2), while the latter displayed slightly higher electron density, suggesting strong electronic coupling between Mn_{SA} and Pt_{NP} (Figure 4e). This interaction was further rationalized by the rectifying Mott-Schottky

© 2025 Wiley-VCH GmbH

16136829, 2026, 6, Downloaded from https://onlinelibrary.wiley.com/doi/10.1002/smll.202512014 by Jeonbuk National University, Wiley Online Library on [18/10/2026]. See the Terms and Conditions (https://onlinelibrary.wiley.com/terms-and-conditions) on Wiley Online Library for rules of use; OA articles are governed by the applicable Creative Commons License

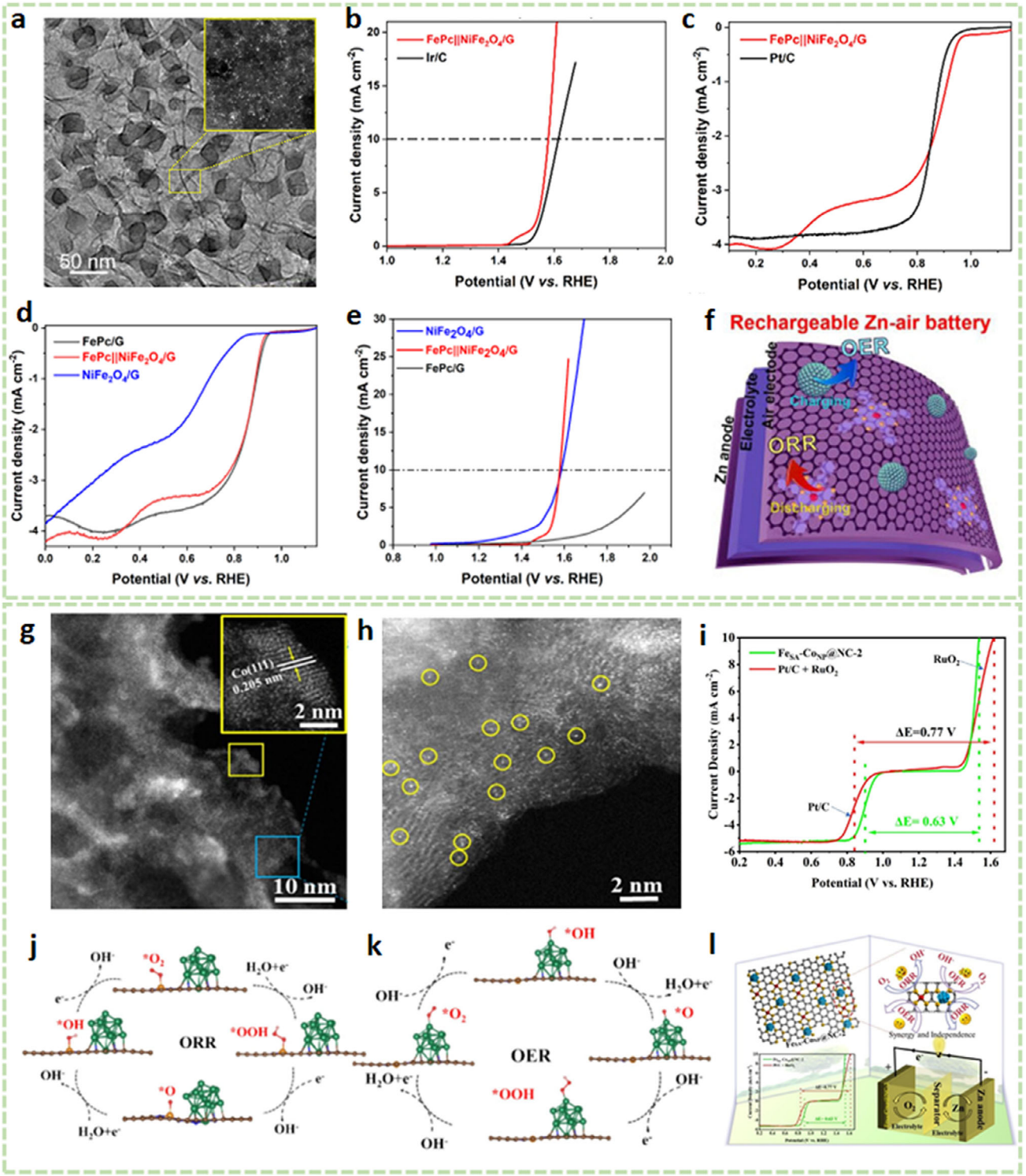


Figure 2. Atomi resolution TEM image of FePc||$NiFe_2O_4$/G The inset shows a region containing only FePc single atoms. b) ORR and c) OER polarization curve of FePc||$NiFe_2O_4$/G and Pt/C. d) ORR and e) OER of FePc/G, $NiFe_2O_4$/G, FePc||$NiFe_2O_4$/G. f) The parallel synergistic effect for ORR/OER of FePc||$NiFe_2O_4$/G catalyst. Reproduced with permission.[59] Copyright 2023, Elsevier. g, h) HAADF-STEM image of Fe_{SA}-Co_{NP}@NC-2, i) The overall LSV curves of Fe_{SA}-Co_{NP}@NC-2 and the mixture of Pt/C + RuO_2 catalysts, j, k) proposed ORR and OER mechanisms of FeN_4-Co NPs model, respectively and l) the scheme illustrates the parallel synergistic effect of Fe_{SA}-Co_{NP}@NC-2. Reproduced with permission.[60] Copyright 2025, Elsevier.

© 2025 Wiley-VCH GmbH

16136829, 2026, 6, Downloaded from https://onlinelibrary.wiley.com/doi/10.1002/smll.202512014 by Jeonbuk National University, Wiley Online Library on [18/10/2026]. See the Terms and Conditions (https://onlinelibrary.wiley.com/terms-and-conditions) on Wiley Online Library for rules of use; OA articles are governed by the applicable Creative Commons License

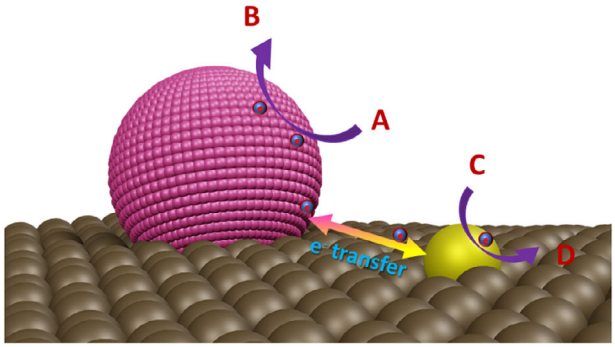


Figure 3. Electronic interaction synergistic effect by electron transfer between SAs and NPs

effect, where the higher work function (E_Φ) of Mn_{SA}/C facilitates electron transfer from Pt_{NP} to Mn_{SA}/C, thereby lowering the Fermi level (E_F) of the composite system (Figure 4f). Consequently, the electron density of Pt_{NP} decreases, highlighting the significant electronic interplay between the two active components (Figure 4g). Additionally, $Fe_{NPs}/MnFe_{SAs}$-NC-25 catalyst was synthesized by Bai et al.[72] for ORR (Figure 4a) and the role of Fe NPs and Mn/Fe SA in this catalyst system was study through DFT calculations. They found that this combination effectively boosts the ORR in alkaline media with the half-wave potential $E_{1/2}$ of 0.91 vs RHE, which surpassed Pt/C (Figure 4h). The DFT calculations revealed that the incorporation of Mn induces a positive shift in the projected density of states (PDOS) peak of Fe, which can enhance surface adsorption capacity for oxygen-containing species. In addition, the d-band center of Fe moves upward in the presence of Mn, resulting in the stronger binding energy between the catalyst and the O-containing species that can reduce the effective electron mass, thus promoting electron migration (Figure 4i,j). Similar electronic interactions have also been observed in non-noble metal hybrid catalysts. For instance, first-principles calculations by Tang et al.[73] demonstrated that the coexistence of transition metals and Fe_6 nanoparticles (Ni-TM-Fe_6 catalyst) regulates the electronic structure of single Ni-N_4 sites, including charge polarization and tuning the d-band center. Consequently, the Ni-TM-Fe_6 structure reduces the free-energy barrier for the key *OOH intermediate during CO_2-to-CO conversion. Likewise, Li et al.[74] reported electron donation from vanadium nitride (VN) nanoparticles to Fe-N_4 sites, thereby modulating the electronic structure of Fe centers. In terms of noble metal-based hybrid systems, Yang et al.[75] introduced a Pt/Meso-Fe_1-NC catalyst exhibiting enhanced ORR activity with an $E_{1/2}$ of 0.915 V and a mass activity of 0.566 A·mg_{Pt}^{-1}. The improvement is ascribed to the electronic modulation between Pt NPs and isolated single Fe atoms, wherein electron transfer from Pt NPs to single Fe atoms occurs. The DFT calculation for the N and supports, Fe_{SA} and Fe_2P_{NP}, showed that P doping led to an up-shift of the d-band center of Fe, thereby facilitating the adsorption of O_2. In this system, the Fe_{SA} served as an electron reservoir, capable of donating or releasing electrons to Fe_2P_{NP}, synergistically enhancing the ORR activity.[76] Notably, the synergistic electronic interactions between Pt-based alloy nanoparticles (e.g., PtNi, PtCo) and SA sites,[76–80] as well as insertion chemistry,[81] have also been shown to be promising strategies for modulating the electronic structure of metals, thereby optimizing catalytic performance.

In a recent study, our group[82] developed a facile and rapid photochemical deposition strategy to incorporate Au SAs into an N-doped carbon matrix, which served as a charge redistribution support to modulate the electronic structure of Pt-Ni alloy NPs. The introduction of Au SAs effectively tuned the electronic environment of the Pt-Ni alloy interfacial charge transfer and d-band engineering, thereby enabling enhanced catalytic activity and durability. DFT calculations (**Figure** 5a–c) confirmed that the formation of stable Au-N_4 coordination sites within the carbon matrix effectively alters the electronic environment of the adjacent Pt-Ni alloy. Specifically, the Au-N_4 sites elevate the d-orbital energy levels of Pt–Ni toward the Fermi level (Figure 5d), thus modulating the catalytic behavior. As a result, the unique $PtNi_{NPs}$/Au-N_4 hybrid structure significantly lowers the energy barrier for *OH adsorption in the rate-determining step (RDS) in ORR (Figure 5e), while also weakening the *H adsorption (Figure 5f), thereby enhancing both ORR and HER activity. A similar stabilizing phenomenon via electronic synergistic effect was also recently identified by Ishiki by Mössbauer spectroscopy analysis.[83] In a related study, Sun et al.[84] have proposed an inducing electron delocalization strategy in which Fe SAs act as electronic regulators to tailor the electronic structure of Au nanocluster through an M-N_x-C coordination. DFT calculations revealed that the introduction of Au nanoclusters induces an upward shift of the Fe_1NC *d*-band center toward the Fermi level in the Au-Fe_1NC system. This shift results in a higher electron density near the Fermi level compared to Fe_1NC, thereby facilitating more efficient electron transfer. Consequently, the Au-Fe_1NC exhibits a more moderate adsorption strength for H_2O, optimizing the balance between adsorption and desorption steps during the HER process. This electronic modulation accounts for the enhanced alkaline water-splitting activity observed for Au-Fe_1NC compared with pristine Fe_1NC. A similar phenomenon was also reported in the Ru/Co@OG system for HER. The modification of O-doped graphene substrate with single metal atoms can effectively enhance the electronic metal-support interaction with the Ru nanoparticles supported on it and redistribute the electrons of Ru nanoparticles, resulting in optimized adsorption free energy of H* species on Ru particles and enhanced HER activity.[85] Other SA-NP hybrid systems have also been recently reported to exhibit electronic synergistic effects that enhance electrocatalytic performance.[86–90] Moreover, the N-doped carbon support fundamentally modulates the d-band center of both SAs and NPs through electronic metal-support interactions (EMSI), enabling asymmetric d-band positioning that optimizes each phase independently. For example, Qui et al.[91] demonstrated that EMSI between single Pd atoms and the N-doped carbon substrate enhances electron transfer at their interface, which decreases charge transfer from Pd nanoparticles to the substrate, thereby reducing the adsorption strength of CO on the metallic Pd nanoparticle sites and optimizing electrocatalytic performance. Xu et al.[92] reported a correlation between N-species, d-band center, work function, and catalytic activity. They demonstrated that the ratio of (pyridinic-N + pyrrolic-N)/graphitic-N modulates the work function and d-band center of metal nanoparticles. By tuning this ratio through

 © 2025 Wiley-VCH GmbH

16136829, 2026, 6, Downloaded from https://onlinelibrary.wiley.com/doi/10.1002/smll.202512014 by Jeonbuk National University, Wiley Online Library on [18/10/2026]. See the Terms and Conditions (https://onlinelibrary.wiley.com/terms-and-conditions) on Wiley Online Library for rules of use; OA articles are governed by the applicable Creative Commons License

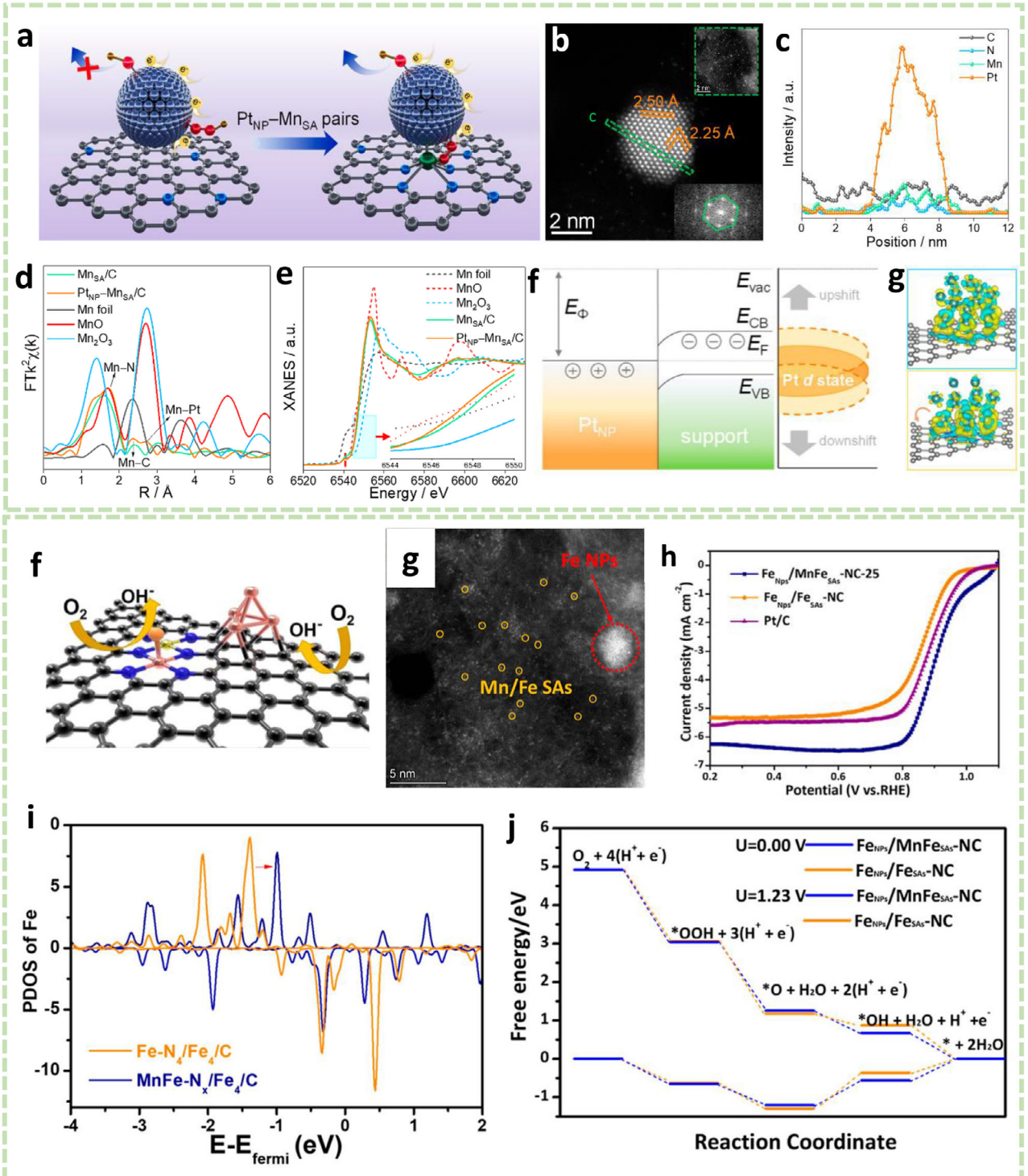


Figure 4. a) Schematic illustration of the electronic synergistic effect of Pt_{NP}-Mn_{SA}/C. b) High-magnification HAADF-STEM images of Pt_{NP}-Mn_{SA}/C in the region of Pt_{NP}, the inset shows the carbon substrate near Pt_{NP}. c) Elemental line profiles (C, N, Mn, and Pt) of Pt_{NP}-Mn_{SA}/C. d) Fourier-transformed k^2-weighted Mn K-edge EXAFS spectra and e) XANES spectra of Pt_{NP}/C, Pt_{NP}-Mn_{SA}/C and standard samples. f) Schematic diagram of the Mott-Schottky junction between Pt_{NP} and support. Evac: vacuum energy after contact with Pt_{NP} and support. The charge density difference of Pt_{NP}/C (top) and Pt_{NP}-Mn_{SA}/C (bottom). The yellow and cyan regions represent electron accumulation and depletion, respectively. Reproduced with permission.[71] Copyright 2024, American Chemical Society. f) The schematic represents the structure of Fe_{NPs}/$MnFe_{SAs}$-NC-25. g) HAADF–STEM images Fe_{NPs}/$MnFe_{SAs}$-NC-25. h) LSV curves of Fe_{NPs}/$MnFe_{SAs}$-NC-25, Fe_{NPs}/Fe_{SAs}-NC and Pt/C. Catalytic activity evaluation by DFT calculations. i) projected density of states (PDOS) of Fe, j) pathways for Fe_{NPs}/$MnFe_{SAs}$-NC-25 and Fe_{NPs}/Fe_{SAs}-NC at U = 0 and 1.23 V. Reproduced with permission.[72] Copyright 2022, American Chemical Society.

 © 2025 Wiley-VCH GmbH

16136829, 2026, 6, Downloaded from https://onlinelibrary.wiley.com/doi/10.1002/smll.202512014 by Jeonbuk National University, Wiley Online Library on [18/10/2026]. See the Terms and Conditions (https://onlinelibrary.wiley.com/terms-and-conditions) on Wiley Online Library for rules of use; OA articles are governed by the applicable Creative Commons License

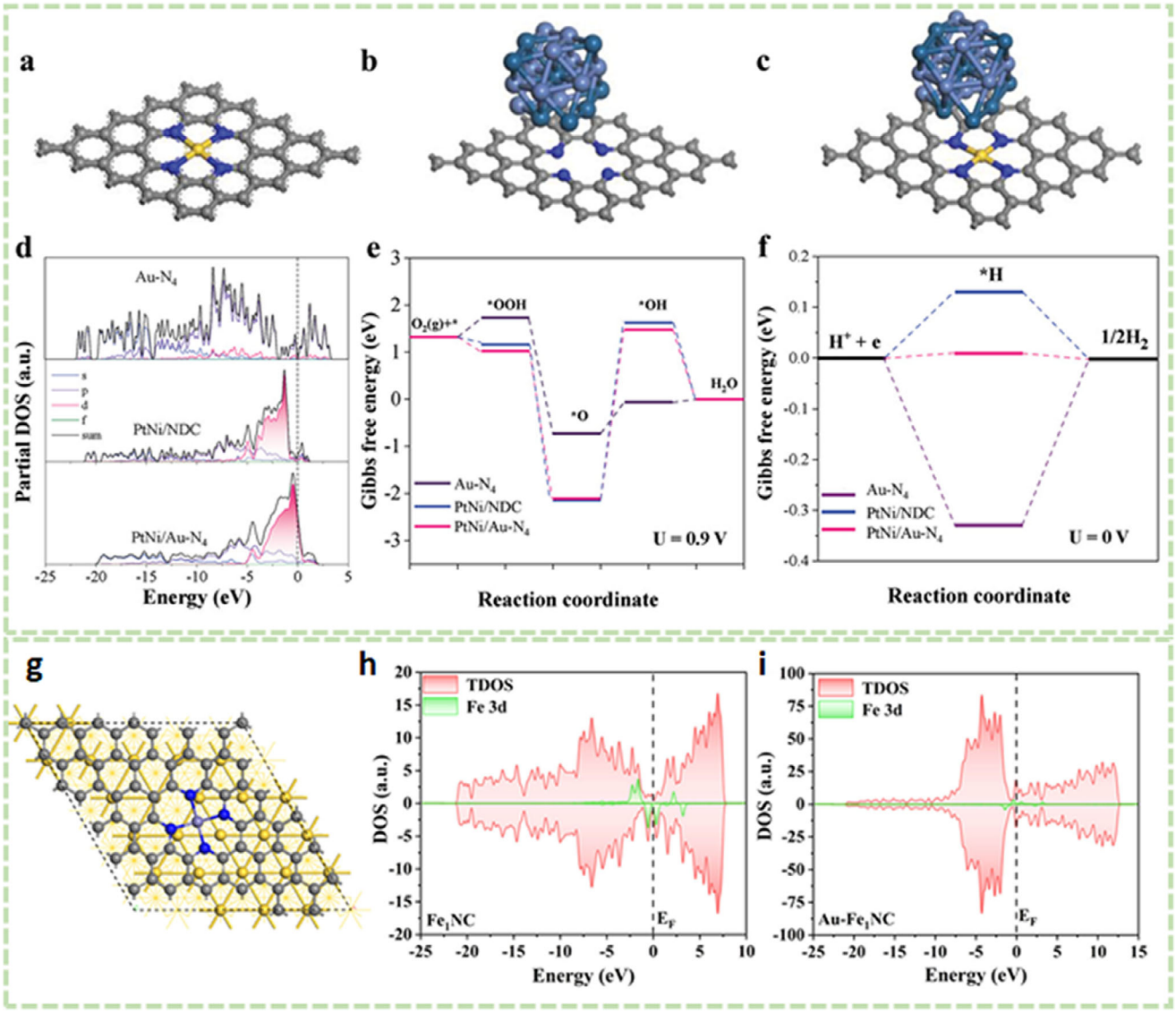


Figure 5. Density functional theory calculations. The structural slab models in the DFT calculations: a) Au-N_4, b) Pt-Ni alloy, and c) Pt-Ni alloy cluster decorated on Au-N_4 nanosheet. Color code: Pt (dark blue), Ni (dark cyan), Au (yellow), C (gray), and N (blue). d) The calculated partial density of state (PDOS), the dark line denotes the position of the Fermi level. The Gibbs free energy diagrams for e) ORR and f) HER pathway correspond to these slab models. Reproduced with permission.[82] Copyright 2024, Wiley-VCH GmbH. g) Top view of the optimized atomic structure model of Au-Fe_1NC. h) Density of states (DOS) of the Fe_1NC model and i) the Au-Fe_1NC model. Reproduced with permission.[84] Copyright 2023, American Chemical Society.

controlled carbonization temperature, they identified an optimal ratio of 1.33 that exhibited the lowest overpotential for HER.

The synergistic electronic interaction between SAs and NPs plays a crucial role in enhancing catalytic capabilities. This interaction effectively modulates and boosts the adsorption strength of reactant species and intermediates, thereby altering the geometry of the reaction pathway. These studies pave the way to a detailed exploration of catalytic reaction mechanisms at the atomic level and offer a viable approach for controlling the activity and stability of metal species in electrocatalysis.

2.3. Tandem Synergistic Effect

Tandem catalysis represents a sophisticated synergistic mechanism where SAs and NPs act sequentially to accomplish multistep reactions.[55,93] In this approach, different active sites are responsible for different elementary steps of the overall reaction pathway, creating a relay-like catalytic process (**Figure 6**). Most of the electrocatalytic reactions (ORR, HER, OER, NRR, etc.) usually involve multiple reaction steps. The activity and selectivity of the electrocatalytic processes are essentially determined by the energy barrier at the RDS among the intermediates created in these multiple reaction steps.[94] The catalytic performance of single

© 2025 Wiley-VCH GmbH

16136829, 2026, 6, Downloaded from https://onlinelibrary.wiley.com/doi/10.1002/smll.202512014 by Jeonbuk National University, Wiley Online Library on [18/10/2026]. See the Terms and Conditions (https://onlinelibrary.wiley.com/terms-and-conditions) on Wiley Online Library for rules of use; OA articles are governed by the applicable Creative Commons License

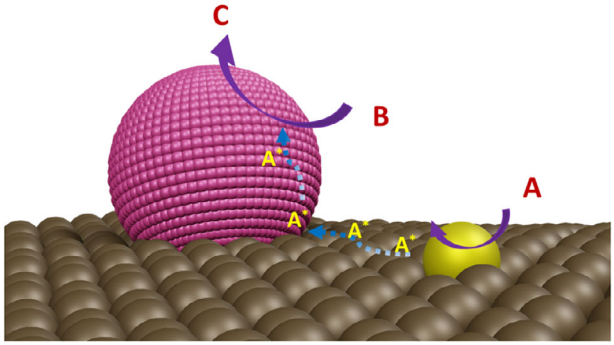


Figure 6. Tandem synergistic effect between supported SAs and NPs

active-center catalysts for multi-step reactions is not ideal. This is because the chemical structure of the catalytic center is relatively simple, and it is difficult to optimize the binding energy of an intermediate without affecting other intermediates.[95,96] Therefore, the integration of SAs and NPs as multiple active sites into a catalyst has been demonstrated to synergistically accelerate the multi-step reactions, enhancing both reaction kinetics and overall catalytic efficiency.[97]

For instance, in the context of alkaline HER, Cao et al.[98] developed a catalyst featuring atomically dispersed Ru SAs (Ru SA-5) in combination with Ru oxide nanocluster (≈1.5 nm) for accelerated HER performance (**Figure** 7a). The DFT simulation indicated that the coupling sites of clusters and atoms are most favorable for the adsorption and dissociation of H_2O compared to the separate cluster and the standalone Ru-C_5 site (Figure 7b,c). First, the freestanding H_2O is captured by Ru SA-5. The adjacent Ru oxide clusters then facilitate efficient H_2O dissociation, as their surface oxygen atoms strongly bind the hydrogen and hydroxyl groups, promoting the cleavage of the O—H bond. Afterward, the hydrogen atoms produced from this step migrate (via hydrogen spillover) to Ru SA-5 sites, where their weaker hydrogen binding energy accelerates the final H_2 desorption, thereby completing the HER cycle (Figure 7d). Zhang et al.[99] prepared CuO/Ni SA tandem catalyst for CO_2RR toward multicarbons (C_{2+}). In this tandem catalyst system, the authors proposed a CO_2RR mechanism analogous to a C_{2+} production factory, where Ni SAs and CuO NPs function as "workers" independently catalyzing the CO_2-to-CO and CO-to-C_{2+} conversions, respectively. The authors designed three catalyst configurations to probe the tandem effect: i) a physical mixing strategy (CuO/N-C + Ni SAs/N-C), where CuO and Ni SAs were separately supported on N-C and physically mixed; ii) a layer-by-layer strategy (CuO/N-C||Ni SAs/N-C), where each component was sequentially sprayed to form a stacked structure; and iii) an adjacent nanostructure strategy (CuO/Ni SAs + N-C), where CuO and Ni SAs were co-loaded with intimate contact (Figure 7e–g). CO_2RR experiments revealed that strategy iii) exhibited superior C_{2+} Faradaic efficiency (Figure 7h) and current density (j_{C2+}) due to the short diffusion path between Ni and Cu sites (Figure 7k), allowing CO generated at Ni SAs to be rapidly consumed by adjacent Cu sites. This configuration minimizes CO loss to the electrolyte and enhances CO utilization (Figure 7j), whereas in strategy i), the greater spatial separation leads to slower CO transfer, partial CO escape into the gas diffusion electrode, and lower C_{2+} product selectivity. For the layer-by-layer system, CO diffusion across the CuO/N-C layer is limited by the much lower CO diffusion coefficient in water (2.1×10^{-9} m^2 s^{-1})[100] compared to the GDE (1.9×10^{-5} m^2 s^{-1}),[101] which restricts CO_2 and CO mass transport under high current densities-evidenced by increased H_2 evolution (Figure 7i) and reduced C_{2+}product FE. Similarly, Chen et al.[102] synthesized an electrocatalyst comprising a Cu site co-coordinated with N and S anchored carbon matrix (Cu-S_1N_3) and an atomically dispersed Cu clusters (Cu_x) electrocatalyst. The unsymmetrical Cu-S_1N_3 atomic interface in the carbon basal plane exhibited an optimized binding energy for the key *COOH intermediate, while the adjacent Cu_x facilitated the protonation of $^*CO^{2-}$ by accelerating water dissociation and supplying $^*H$ to the Cu-S_1N_3 active sites. Zhu et al.[103] reported that cooperatively of Pt_{SAs} with Pt_{NPs} can exhibit the tandem effect for excellent HER performance. In this system, Pt_{NPs} promote water dissociation into $^*H$ and $^*OH$, with the generated $^*H$ species spilling over to adjacent Pt_{SAs}, where H—H bond formation occurs, facilitating the evolution of gaseous H_2. Guo et al.[104] reported a novel NH_3-promoted dealloying strategy to prepare a closely packed hybrid electrocatalyst containing Pt-based alloy nanocrystals and dense isolated single Ni sites. This hybrid architecture, donated as $Pt_{1.5}Ni_{1-x}$/Ni-N-C, exhibited a clear tandem synergistic effect during ORR. The catalyst demonstrated exceptional ORR performance, achieving a mass activity of 4.10 A mg^{-1}_{Pt} in half-cell measurement and a peak power density of 1.72 W cm^{-2} in H_2/O_2 fuel cell test. Mechanistic investigations revealed that the hybrid structure ensures the reduction of two $2e^-$ at Ni SAs, and the corresponding intermediate (OOH^*) rapidly migrates to the neighboring Pt-based NC to decompose into O^* and OH^*. The mutual assistance of the PtNi cluster and Ni-N-C together completes a $4e^-$ route, realizing the tandem catalytic effect for ORR, in which distinct steps of the overall reaction are handled by different active centers (**Figure** 8a,b). Moreover, the more abundant electronic states near the Fermi-level over $Pt_{1.5}Ni_{1-x}$/Ni-N-C than over $Pt_{1.5}$Ni/N-C indicate the possible electron interaction between the Pt-Ni clusters and the Ni-N-C sites, which helps to achieve an enhanced catalytic performance (Figure 8c). In another work, a similar hybrid structure catalyst (L1-PtCo/Co-N-PCNF) was reported by Lai et al.[105] that also exhibited the tandem synergistic effect in ORR. The synthesis was initiated by electrospinning to form Co-N_4/C porous fiber. Afterward, the L1-PtCo/Co-N-PCNF composite electrode was formed after deposition of Pt NPs on the Co-N-PCNF and subsequent thermal annealing. The composite electrode exhibited excellent ORR activity and durability in a H_2-air fuel cell. The theoretical results suggested the oxygenated intermediates are more easily reduced to H_2O_2 at Co-N_4/C sites. In the presence of L1-PtCo/Pt sites, the H_2O_2 formed at the Co-N_4/C site could quickly transfer to the neighboring L1-PtCo/Pt alloy NPs and be further reduced to H_2O.

3. Carbon-Based Materials Supported SAs and NPs Hybrid Electrocatalysts

In electrocatalysis, although several factors, including reaction type, metal loading, spatial arrangement, and the physicochemical nature of the support, affect catalyst performance, we believe that the physicochemical characteristics of the support play the

 © 2025 Wiley-VCH GmbH

16136829, 2026, 6, Downloaded from https://onlinelibrary.wiley.com/doi/10.1002/smll.202512014 by Jeonbuk National University, Wiley Online Library on [18/10/2026]. See the Terms and Conditions (https://onlinelibrary.wiley.com/terms-and-conditions) on Wiley Online Library for rules of use; OA articles are governed by the applicable Creative Commons License

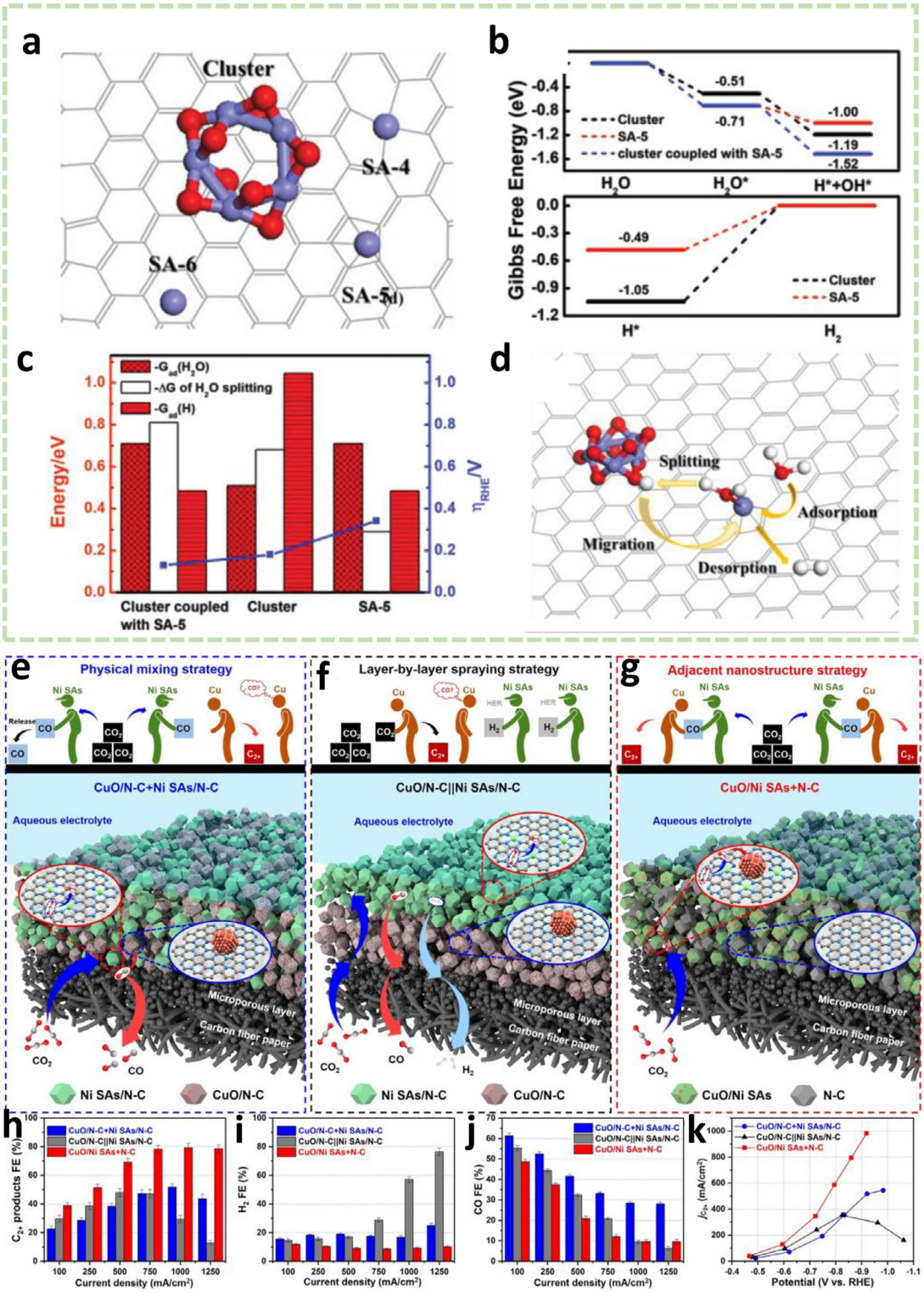


Figure 7. a) Top view of a graphene-supported Ru_5O_{10} cluster surrounded by Ru SAs. b) Free energy diagrams for H_2O adsorption-decomposition and H_2 desorption on various active sites. c) Comparison of experimental and calculated results, including H_2O and H desorption energies, H_2O splitting reaction heat on Ru_5O_{10}, SA-5, and Ru_5O_{10}-SA-5, alongside experimental alkaline HER overpotential. d) Schematic illustration of the synergistic alkaline HER pathway between Ru oxide clusters and Ru single atoms. Reproduced with permission.[98] Copyright 2021, Wiley-VCH GmbH. The working mechanism schematics for tandem catalyst electrodes fabricated with strategies of physical mixing (e), layer-by-layer spraying (f), and adjacent nanostructure (g). The comparisons of tandem catalyst electrodes fabricated with three strategies in C_{2+} product FE (h), H_2 FE (i), CO FE (j), and partial current densities of C_{2+} products (k). Reproduced with permission.[99] Copyright 2025, Elsevier.

© 2025 Wiley-VCH GmbH

16136829, 2026, 6, Downloaded from https://onlinelibrary.wiley.com/doi/10.1002/smll.202512014 by Jeonbuk National University, Wiley Online Library on [18/10/2026]. See the Terms and Conditions (https://onlinelibrary.wiley.com/terms-and-conditions) on Wiley Online Library for rules of use; OA articles are governed by the applicable Creative Commons License

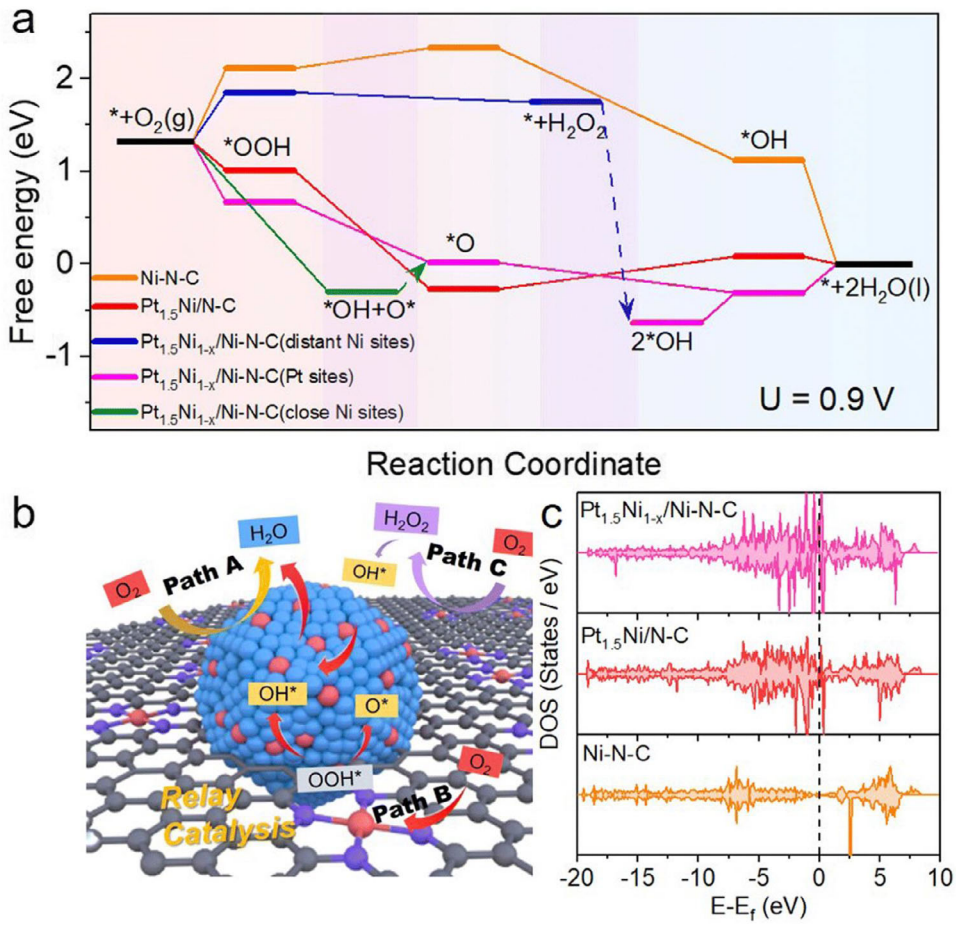


Figure 8. a) The ORR free energy diagram of Ni-N-C, $Pt_{1.5}Ni$/N-C, $Pt_{1.5}Ni_{1-x}$/Ni-N-C with distant Ni sites, close Ni sites and Pt sites, b) the schematics of $Pt_{1.5}Ni_{1-x}$/Ni-N-C (blue, red, purple, and gray spheres present Pt, Ni, N and C atoms, respectively), c) the total density of states and the corresponding d band centers of $Pt_{1.5}Ni_{1-x}$/Ni-N-C, $Pt_{1.5}Ni$/N-C and Ni-N-C. The Fermi level is marked with a black dashed line. The d band center is marked with a purple line. Reproduced with permission.[104] Copyright 2025, RSC Publishing.

most important role in governing the synergistic interactions between SAs and NPs. This is primarily because the support fundamentally determines the stability, electronic structure, and spatial proximity of the active sites, all of which are crucial for facilitating effective synergy.

Metal loading and spatial arrangement influence the active site density and proximity, but these parameters are often constrained or enabled by the support's ability to effectively anchor and disperse metal species. Similarly, the reaction type dictates which synergistic mechanism (parallel, electronic interaction, or tandem) will dominate; however, the realization and efficiency of these mechanisms are largely dependent on the structural and electronic properties of the support. Generally, the isolated metal atom immobilized on the appropriate supports has a well-known geometric configuration, electronic structure and 100% atom utilization efficiency, which can catalyze the conversion of reactants to the desired products.[106–108] However, in the SAs-NPs systems, due to the high surface free energy of SAs-NPs tend to agglomerate during the preparation process or catalytic application. Thus, synthesizing stable SAs-NPs materials poses a significant challenge. For electrochemistry catalysts, carbon-based nanomaterials serve as excellent supports for SAs and NPs because of their large specific surface area, high conductivity, and rich surface defects.[109] Notably, nitrogen (N)-doped carbon represents the largest class of supports due to the lone electron pairs on N atoms, which exhibit strong coordination abilities with metal species, forming robust metal-nitrogen (M-N) coordination bonds and establishing strong interactions between SAs (or NPs) and the carbon support. These interactions have been demonstrated to enhance the thermal and chemical stability of the systems.[110,111] Given these advantages, engineering N-doped carbon supports with precise nitrogen speciation and defined porous architectures has become a central focus, requiring systematic exploration of synthesis methodologies. Therefore, this section summarizes recent advances in the synthesis of nitrogen-containing carbon-based support for SAs and NPs systems. Methods for the synthesis of N-doped carbons are covered, including 1) synthesis using N-doping precursors (e.g., urea, imidazole, melamine), 2) synthesis of MOF-derived carbon, and 3) template-assisted method for ordered porous N-doped carbons.

© 2025 Wiley-VCH GmbH

16136829, 2026, 6, Downloaded from https://onlinelibrary.wiley.com/doi/10.1002/smll.202512014 by Jeonbuk National University, Wiley Online Library on [18/10/2026]. See the Terms and Conditions (https://onlinelibrary.wiley.com/terms-and-conditions) on Wiley Online Library for rules of use; OA articles are governed by the applicable Creative Commons License

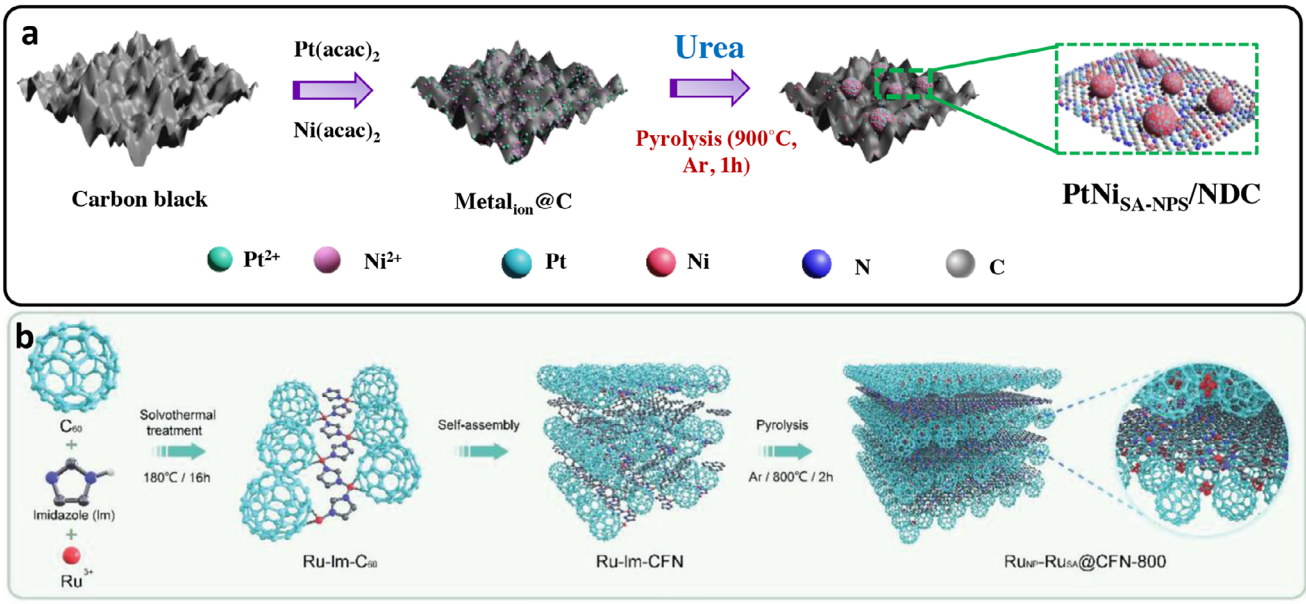


Figure 9. a) Schematic illustration of the preparation process of the $PtNi_{SA\text{-}NPS}$-NDC electrochemical catalysts. Reproduced with permission.[115] Copyright 2023, Elsevier. b) Schematic illustration of the synthetic process of Ru_{NP}-Ru_{SA}@CFN-800. Reproduced with permission.[118] Copyright 2023, Wiley-VCH GmbH.

3.1. Pyrolysis Carbon with Secondary Nitrogen Sources

In this method, catalyst materials are usually synthesized through the pyrolysis of a mixture containing inorganic metal salts, carbon and reactive nitrogen sources such as urea, imidazole or melamine at high temperature in inert environments. During the pyrolysis process, inorganic metal salts convert to metal SAs or NPs, while nitrogen atoms are doped into the carbon structure, forming various nitrogen functionalities including pyridinic-N, graphitic-N, pyrrolic-N and metal-N_x single active sites.[112] These special structures can enhance the content of active sites, improve the charge transfer process, and increase the electrocatalytic performance through synergistic effects.[113,114]

Our group has recently reported a Pt-Ni alloy NPs and SAs (Pt, Ni) anchored on N-doped carbon support ($PtNi_{SA\text{-}NPS}$/NDC) using urea as a reactive nitrogen source,[115] shown in **Figure 9a**. The activated carbon was initially used to adsorb Pt^{2+} and Ni^{2+}. After drying, the mixture was finely ground with a suitable amount of urea, followed by the pyrolysis process at 900 °C for 1h in an Ar atmosphere. Based on the XPS and EXAFS results, we concluded that the high proportion of pyridinic-N originated from the decomposition of urea during the pyrolysis process. The resulting pyridinic-N sites effectively anchor and stabilize the Pt and Ni single atoms within the carbon matrix. This was demonstrated by the notably higher percentage of single atoms found in the material with N-doping compared to the sample without N-doping. The obtained hybrid structure catalyst exhibited superior electrocatalytic activity toward ORR ($E_{1/2}$ = 0.912 V) and enhanced Pt utilization ($0.033 g_{Pt} kW^{-1}$) in PEMFCs. The utilization of urea as a nitrogen-doping precursor has also been reported for Pd SAs and Pd NPs systems for electrocatalytic oxidation of methanol.[116]

Liu et al.[117] reported the partial reconstruction of Pt SAs into Pt NPs on N-doped carbon for ORR. First, Black Pearl carbon was grounded with melamine as a reactive nitrogen source. The mixture was pyrolyzed at 650 °C for 1h in an Ar atmosphere to form N-doped carbon (NBP). The Pt SAs were deposited through a hydrothermal ethanol reduction reaction, and they showed high selectivity for the $2e^-$ ORR path. By reconstructing the coordination environment of isolated Pt atoms through a high-temperature pyrolysis process, ≈48% of Pt SAs can be retained in the form of single-neighbor pyridinic-nitrogen-anchored SA Pt active centers (Pt_1-N_{Pd}) for highly active and stable $4e^-$ oxygen reduction pathways.

Luo and coworkers[118] introduced a lattice-confined in situ reduction effect of the 3D carbon fullerene network (CFN) to trap Ru_{NPs} and using imidazole as a nitrogen source to stabilized Ru_{SAs} (Figure 9b). The Ru-Im-CFN precursor was first prepared by the solvothermal method followed by the pyrolysis at 800 °C for 2h under an Ar atmosphere. The EXAFS R-space fitting results showed that the coordination number of Ru NPs is 12, while it is 3.6 for the Ru-N coordinate. The obtained Ru_{NP}-Ru_{SA}@CFN-800 catalyst exhibited outstanding electrocatalytic HER performance with an overpotential of 33 mV at 10 mA cm^{-2} and a robust durability for 1400 h. This lattice-confined in situ reduction strategy can guide a rational design of novel and efficient electrocatalysts.

As mentioned above, the doping of nitrogen into the carbon matrix using the pyrolysis secondary nitrogen method can generate various chemical functionalities. However, this conventional method typically results in nitrogen incorporation primarily only into the edges of the carbon material or defects of the carbon matrix. This localized doping may limit the overall efficiency of forming uniformly distributed M-N_x-C active sites, thereby constraining the optimization of catalytic performance.

© 2025 Wiley-VCH GmbH

16136829, 2026, 6, Downloaded from https://onlinelibrary.wiley.com/doi/10.1002/smll.202512014 by Jeonbuk National University, Wiley Online Library on [18/10/2026]. See the Terms and Conditions (https://onlinelibrary.wiley.com/terms-and-conditions) on Wiley Online Library for rules of use; OA articles are governed by the applicable Creative Commons License

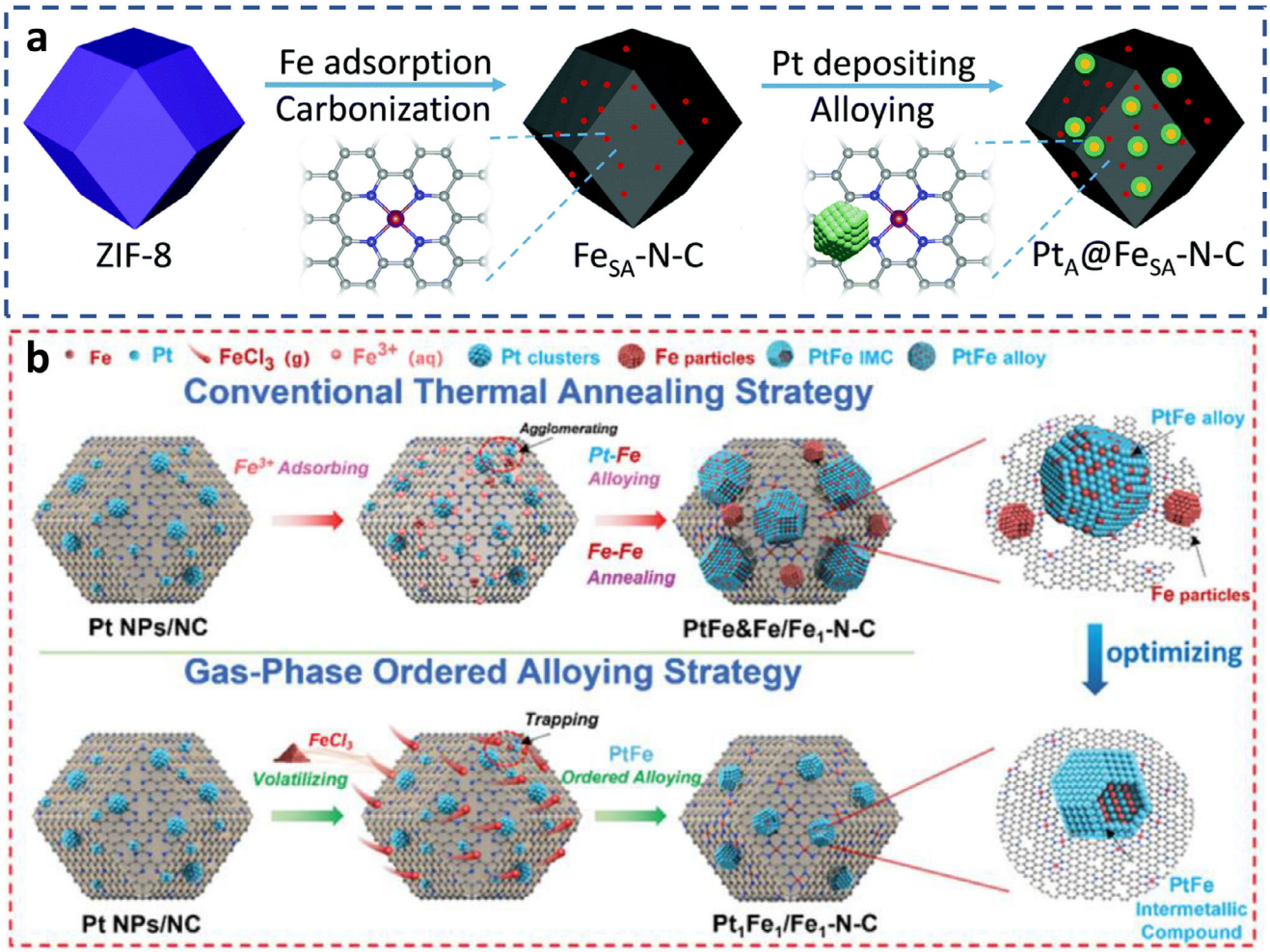


Figure 10. a) Schematic illustration of the preparation of Pt_A@Fe_{SA}-N-C. Reproduced with permission.[126] Copyright 2020, RSC Publishing. b) Schematic illustration of gas-phase ordered alloying strategy for the preparation of Pt_1Fe_1/Fe_1-N-C and conventional thermal annealing strategy for the preparation of contrast sample PtFe&Fe/Fe_1-N-C. Reproduced with permission.[130] Copyright 2023, Wiley-VCH GmbH.

3.2. MOF-Derived Carbon

MOFs are crystalline porous materials composed of metal ions or clusters coordinated to organic ligands, forming periodic 3D networks.[119,120] In recent years, MOFs have been used as useful precursors/templates to prepare single-atom catalyst materials via pyrolysis due to their adjustable porous structure, chemical properties, and abundant nitrogen source.[121] Further, in order to avoid the accumulation of metal centers, the sacrificial metal of bimetallic MOF is commonly applied as the N-C material substrates. Among them, zeolite imidazolate framework (such as ZIF-8, ZIF-67) is most commonly used as a template, where the Zn^{2+} ion acts as metal nodes and complexes with the organic ligand of 2-methyl imidazole to form stable structures. During pyrolysis, the nitrogen source contained in MOFs and metal can form an M-N_x coordination, which is well-known to improve the thermal and chemical stability of single-atom catalysts (SACs). Notably, the nitrogen configurations (such as pyrrolic-N, pyridinic-N, and graphitic-N) can be precisely tuned by controlling the pyrolysis temperature.[122] Typically, the pyrolysis temperature for MOF-derived carbon materials ranges from 600 to 1100 °C. As the pyrolysis temperature increases, the relative content of pyridinic-N decreases, while that of graphitic-N increases.[123–125] This evolution not only influences the anchoring and stabilization of SAs or NPs but also affects the electron transfer kinetics during electrochemical processes. Therefore, both the pyrolysis temperature and duration should be carefully optimized to achieve the desired catalytic performance. Furthermore, at high pyrolysis temperatures, zinc metal vaporizes, which not only inhibits metal aggregation but also promotes the formation of a highly porous carbon architecture. This porosity improves the accessibility of active sites, facilitating efficient mass transport and reactant diffusion. Thus, understanding the mechanism of MOF-derived carbon support is critical for the rational design and development of novel SAs-NPs catalyst systems.

For instance, Ao et al.[126] used ZIF-8 as a host matrix to adsorb Fe ions (**Figure 10a**). Following the carbonization at 900 °C for 2h, the resulting Fe_{SA}-N-C was subsequently used as a substrate for depositing Pt NPs. The final product Pt_A@Fe_{SA}-N-C was obtained

© 2025 Wiley-VCH GmbH

16136829, 2026, 6, Downloaded from https://onlinelibrary.wiley.com/doi/10.1002/smll.202512014 by Jeonbuk National University, Wiley Online Library on [18/10/2026]. See the Terms and Conditions (https://onlinelibrary.wiley.com/terms-and-conditions) on Wiley Online Library for rules of use; OA articles are governed by the applicable Creative Commons License

by an annealing treatment process, which results in alloying of Pt and Fe atoms to form a highly ordered core-shell Pt_3Fe intermetallic structure. HAADF-STEM images demonstrated that the core-shell NPs were uniformly formed and individually distributed on the Fe_{SA}-N-C support. Extended X-ray absorption fine structure (EXAFS) analysis revealed that Fe atoms were coordinated with four N atoms to form a well-defined Fe-N_4 moiety, while no Fe—Fe coordination bonds were detected. The high specific surface area of $Pt_A@Fe_{SA}$-N-C (331 m^2g^{-1}) with a highly porous structure may facilitate mass transfer in electrochemical reactions. The stability test revealed that the presence of Fe in the ZIF-derived carbon enhanced the catalyst stability, as evidenced by an $E_{1/2}$ decrease of only 7 mV for $Pt_{SA}@Fe_{SA}$-N-C compared with 29 mV for Pt_{SA}@N-C. Building on this, further explorations provided a fundamental understanding of the correlation between MOFs templates and N-C materials. In a similar example, Wu and coworkers[127] proposed a ZIF-8-based modification using a carbon nanotube. The isolated binary atomic Co/Fe sites (Fe-N_4 and Co-N_2C_2) were anchored with nitrogen-coordinated Co nanoclusters on CNTs. This spatial arrangement was achieved by precisely controlling the distance between the Fe and Co sites in the MOF structure. The highly conductive CNTs, as a robust support, keep high electrochemically ECSA, low charge mass-transport resistance, and prevent Co clusters from agglomerating. Notably, Fe/Co-CTs/CNT exhibited excellent stability in both acidic and alkaline media, with $E_{1/2}$ decreases of only 12 and 15 mV, respectively, indicating that carbon oxidation was minimal due to the enhanced degree of graphitization. The SAs-NPs supported ZIF-derived intercalated CNT systems were also reported for (Co1→Cop)/N-CNTs by Yang et al.,[128] CNT@Co_{SA}-Co/NCP material by Li et al.,[97] FeS/FeNSC catalyst by Chen et al.[129]

Moreover, the secondary disturbances of the pyrolysis process can also be utilized to prepare M-N_x-C materials. Zhou and colleagues[130] introduced a gas-phase ordered alloying strategy to construct an effective synergistic catalytic system combining PtM intermetallic compounds and densely isolated transition metal site (M-N_4) on NC derived from ZIF-8 (Figure 10b). The Pt NPs/NC was prepared by adsorbing a Pt precursor onto the NC support and annealing it at 350 °C for 0.5 h under H_2/Ar atmosphere. Subsequently, the Pt NPs/NC and $FeCl_3$ were placed separately in two porcelain boats in a tube furnace. The $FeCl_3$ was heated in the upstream of N_2 flowing over the surface of Pt NPs and N-doped carbon to provide a continuous iron source. In this process, some of the Fe species combine with Pt to form PtFe alloy nanoparticles, while the remaining Fe atoms are anchored as isolated SA sites within the N-doped carbon matrix. This secondary disturbance pyrolysis method was also applied to prepare Cu SA captured by N-rich carbon support by pyrolyzing in the upstream NH_3 flow to Cu SAs.[131] ZIF-8 was used as the anchoring substrate to capture the volatile metal species.

Additionally, the abundant nitrogen content and unique pore architecture of MOF-derived carbon supports significantly contribute to enhancing the durability of electrocatalysts. Recently, our group[132] proposed a novel strategy to improve electrocatalyst durability by employing a high-porosity, nitrogen-rich carbon framework (NDCF) as a support. In this design, Pt-Ni alloy NPs, surrounded by a high density of Pt and Ni SAs, were immobilized within the NDCF matrix (**Figure 11**), which collectively exhibited bifunctional electrocatalytic activity and enhanced durability for both HER and ORR. We found that the NDCF support not only provides an enlarged surface area that exposes more intrinsic active sites and maximizes SA anchoring but also enables a uniform distribution of Pt-Ni alloy NPs, ensuring optimal accessibility for catalytic reactions. Furthermore, the exceptional durability of the $PtNi_{SA\text{-}NPs}$/NDCF electrocatalyst is attributed to the high content of pyridinic-N, which stabilizes Pt and Ni atoms within the carbon matrix, and the physical encapsulation of the alloy NPs by a carbon shell, which prevents their dissolution and aggregation during prolonged electrochemical operation. However, MOF-derived carbon offers a promising support for SAs-NPs catalysts; nevertheless, precise control of the SAs/NPs ratio as a function of pyrolysis temperature should be given particular priority to achieve optimal electrocatalytic performance.

3.3. Template-Assisted Method for N-Doped Ordered Porous Carbons

Growing demand to modify and optimize the physicochemical properties of carbon materials for energy storage and conversion applications has created an urgent need to develop advanced structural designs. In this context, ordered porous carbon nanostructures synthesized via the self-assembly of polymer precursors and templating methods allow for precise control of pore structure and geometry. These materials offer uniform pore distribution and improved pore connectivity, which are essential for enhancing electrochemical performance.[133–135]

Carbon precursors containing nitrogen atoms, such as polyaniline, polypyrrole, polyvinylpyrrolidone, polyacrylonitrile, melamine, and nitrogen-rich ionic liquids, are commonly used in combination with hard templates to incorporate nitrogen into the carbon framework of ordered mesoporous carbons. In this approach, the pore size, shape, and degree of structural ordering can be precisely controlled using solid templates,[136] enabling systematic studies on the influence of pore dimensions on the thermal and structural stability of the resulting carbon materials.[137] After carbonization under an inert atmosphere, the template is removed via chemical etching with typically NaOH or HCl. The interconnected pore network present in the composite is transferred into the final N-doped carbon framework, where the space initially occupied by the template is converted into a uniform mesopore. One of the major advantages of N-doped mesoporous carbon is its tunable structure-property relationship, which makes it a highly promising support for SAs and NPs electrocatalysts. The high nitrogen content in these materials facilitates the uniform dispersion of SAs during synthesis. Moreover, the adjustable pore size and shape provide effective confinement for stabilizing NPs during electrochemical processes. Additionally, the shape and size of individual carbon particles can be precisely controlled, enabling the optimization of mass transport and diffusion properties within the catalyst particle for specific electrochemical applications.

Recently, Zeng, Küspert, and co-workers[138] reported the development of mesoporous N-doped carbon (MPNC) spheres as a support for Pt SAs, clusters, and NPs for HER, using a simple wet impregnation method. The MPNC spheres were synthesized via pyrolysis of polyamine-SiO_2 composites at 1000 °C under an inert atmosphere, followed by template removal through

© 2025 Wiley-VCH GmbH

16136829, 2026, 6, Downloaded from https://onlinelibrary.wiley.com/doi/10.1002/smll.202512014 by Jeonbuk National University, Wiley Online Library on [18/10/2026]. See the Terms and Conditions (https://onlinelibrary.wiley.com/terms-and-conditions) on Wiley Online Library for rules of use; OA articles are governed by the applicable Creative Commons License

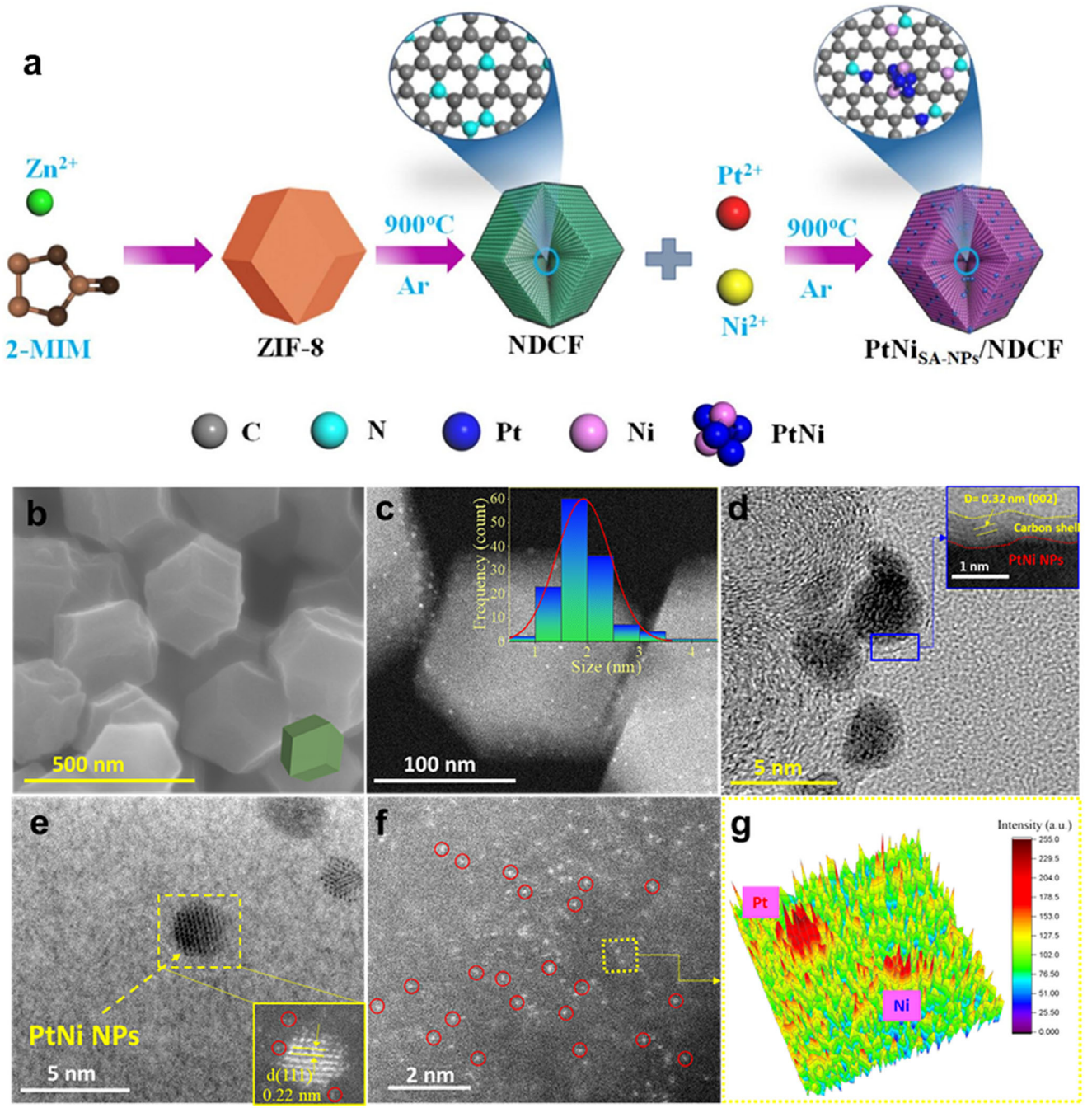


Figure 11. a) Schematic diagram describing the synthetic process followed to develop the $PtNi_{SA\text{-}NPs}$/NDCF catalyst. b) FE-SEM FigureCaptionimage of $PtNi_{SA\text{-}NPs}$/NDCF catalyst. c) low HAADF-STEM images of $PtNi_{SA\text{-}NPs}$/NDCF catalyst, the inset is the size distribution of Pt-Ni alloy NPs. c) High-resolution HAADF-STEM images of $PtNi_{SA\text{-}NPs}$/NDCF catalyst, the inset shows the carbon shell thickness is around 1 nm. d) CS-corrected TEM image of $PtNi_{SA\text{-}NPs}$/NDCF catalyst at an area containing Pt-Ni NPs, along with the crystalline feature of the area indicated by the yellow box. e) HAADF-STEM image of $PtNiS_{A\text{-}NPs}$/NDCF at an area without NPs. f) The intensity profile obtained at the site of the yellow box in (e). sReproduced with permission.[132] Copyright 2024, Elsevier.

HF etching (**Figure** 12). The resulting MPNCs exhibited high monodispersity with an average particle size of 298 ± 23 nm and a uniform mesoporous structure with a pore size of 24 ± 2 nm distributed throughout the entire particle volume. Nitrogen physisorption measurements revealed a high specific surface area of 540 m^2 g^{-1}, with mesopores accounting for 92.8% of the total pore volume. Using wet impregnation, 20 wt.% of Pt was loaded onto both the MPNC and an N-doped carbon nanofiber (CNF) for comparison. The mesoporous structure of MPNC promoted the formation of highly dispersed Pt SAs, clusters, and NPs. The

© 2025 Wiley-VCH GmbH

16136829, 2026, 6, Downloaded from https://onlinelibrary.wiley.com/doi/10.1002/smll.202512014 by Jeonbuk National University, Wiley Online Library on [18/10/2026]. See the Terms and Conditions (https://onlinelibrary.wiley.com/terms-and-conditions) on Wiley Online Library for rules of use; OA articles are governed by the applicable Creative Commons License

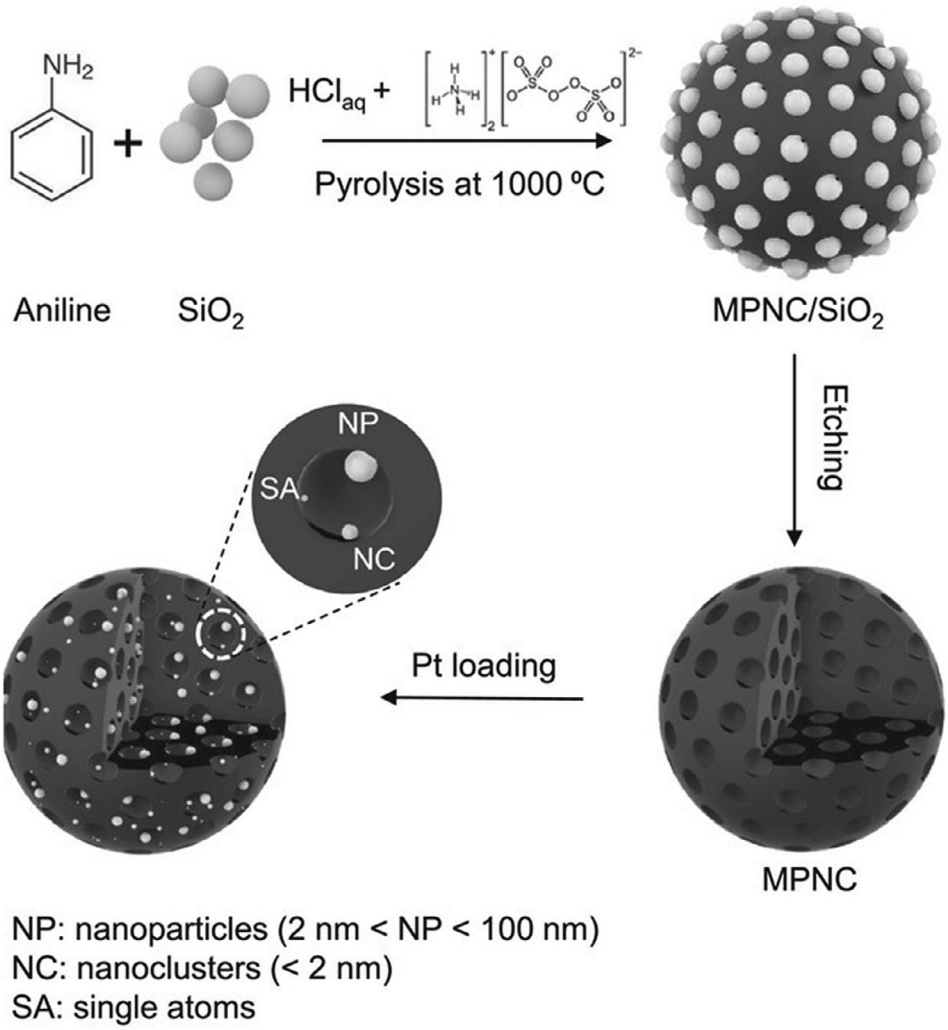


Figure 12. Schematic illustration of the synthesis of highly dispersed Pt entities composed of a mixture of Pt single atoms, clusters, and nanoparticles incorporated into MPNC nanospheres. The high Pt-dispersion achieved results from the mesopore-confinement effects of the support. Reproduced with permission.[138] Copyright 2023, Wiley-VCH GmbH.

Pt/MPNC catalyst exhibited geometric and Pt mass activities for HER that were 4.2 and 26 times higher, respectively, than commercial Pt/C and Pt/CNF catalysts with similar Pt loadings. The enhanced HER performance was attributed to the structural advantages of the MPNC support and the high dispersion of Pt species. Pt single atoms are estimated to contribute ≈65% of the measured current, with the remaining 35% originating from Pt NPs and clusters. Furthermore, Pt/MPNC exhibited an outstanding stability during the chronopotentiometry testing, showing a slight overpotential increase of only 2.6 mV vs. RHE after 8 h of chronopotentiometry test at 10 mA cm^{-2}_{geo} and only 2.8 mV vs. RHE after 8 h at 20 mA cm^{-2}_{geo}.

4. Summary and Future Outlook

The recent advances in electrocatalysis have demonstrated that SACs, with their unique electronic structure and nearly 100% atomic utilization, play a crucial role in electrochemical reactions. Moreover, these SA sites can synergize with NPs to enhance catalytic activity, enrich active site diversity, and improve cost-effectiveness. Since the concept of SACs was first introduced in 2011, numerous synergistic SA-NP catalysts have been reported for electrocatalytic reactions, including ORR, OER, HER, CO_2RR, and NRR. In this review, the synergistic effect between SAs and NPs was summarized and classified into three categories: parallel effect, electron interaction effect, and tandem effect. In a parallel and tandem effect, there are two types of reactions in two-site catalysis, one occurring on SAs and the other on NPs. In electron interaction effects, SAs primarily tune the electronic structure of NPs (or vice versa), thereby altering activity and reaction pathways. We suggest that researchers studying SAC catalysts should not overlook the partial formation of small clusters or NP catalysts. This interplay could significantly impact the catalytic performance due to synergistic effects between them. Furthermore, we emphasize to researchers that these types of

© 2025 Wiley-VCH GmbH

16136829, 2026, 6, Downloaded from https://onlinelibrary.wiley.com/doi/10.1002/smll.202512014 by Jeonbuk National University, Wiley Online Library on [18/10/2026]. See the Terms and Conditions (https://onlinelibrary.wiley.com/terms-and-conditions) on Wiley Online Library for rules of use; OA articles are governed by the applicable Creative Commons License

synergistic effects could also coexist, especially in highly loaded catalytic systems.

This review also highlights synthetic strategies for nitrogen-doped carbon supports that stabilize both SAs and NPs. Incorporating SAs and NPs into pores or matrices helps mitigate Ostwald ripening, agglomeration, and migration. Furthermore, by controlling the N-doping configurations, pore size, porosity, and specific surface area of N-doped carbon materials, insights are provided into the rational design of SAs and NPs hybrid structured catalysts. In particular, nitrogen-enriched ZIF-derived carbon and templated-assist mesoporous N-doped carbon make it a promising support, not only to enhance the durability of SAs and NPs but also to provide a trapping point for M-N_x in gas-phase alloying/dealloying synthesis of PM alloy NPs. Collectively, this review aims to provide insights and design strategies for developing efficient SA–NP hybrid electrocatalysts tailored for energy applications.

In the future outlook, exploring the combination of SAs and NPs can be expanded to encompass various particle types, different diatomic or triatomic configurations, and potentially high-entropy single atoms. Incorporating heteroatoms represents another promising route to enhance intrinsic activity and durability. To unravel the mechanism of synergistic effects, further studies are needed on how the distance between SAs and between SAs and NPs influences performance, requiring more precise control of synthesis strategies. The development of new static or in situ characterization methods for catalysts containing mixtures of SAs and NPs during the reaction process remains a significant challenge and requires more research. Currently, techniques such as HAADF-STEM, XAS, and XPS play significant roles in the characterization of SAs-NPs systems. However, for a more profound comprehension of the reaction mechanisms within these systems, the development of advanced in situ characterization techniques is imperative. Furthermore, cost-effective synthesis routes for scalable catalyst production and industrial application are also essential. Non-carbon supports, such as metal oxides (e.g., CeO_2, TiO_2, NiO) and MXenes, offer complementary advantages in promoting strong metal-support interactions (SMSI) and enhancing electrochemical performance. However, systematic investigations elucidating the influence of different supports on SA-NP synergy remain at a nascent stage of development. Theoretical computation will continue to play a central role in elucidating reaction mechanisms. It is important to mention that theoretical calculations should be consistent with actual experimental data. Integration of computational methods with artificial intelligence (AI) offers a powerful approach to accelerate catalyst discovery and decode complex catalytic phenomena. Careful attention to selecting realistic models will be essential to ensure predictive accuracy and reliability.

Acknowledgements

This work was supported by the BK21-FOUR program of the Ministry of Education and Human-Resource Development, South Korea; the National Research Foundation of Korea (NRF) and the Commercialization Promotion Agency for R&D Outcomes (COMPA) grant funded by the Korea government (Ministry of Science and ICT) (RS-2025-02314407); and the Regional Innovation System & Education (RISE) initiative, funded by the Ministry of Education and administered by the National Research Foundation of Korea (NRF).

Conflict of Interest

The authors declare no conflict of interest.

Keywords

carbon support, catalysts, nanoparticles, single atoms, synergistic

Received: September 30, 2025
Revised: November 15, 2025
Published online: December 15, 2025

[1] X. Tian, X. F. Lu, B. Y. Xia, X. W. (David) Lou, *Joule* **2020**, *4*, 45.
[2] M. Tahir, L. Pan, F. Idrees, X. Zhang, L. Wang, J. J. Zou, Z. L. Wang, *Nano Energy* **2017**, *37*, 136.
[3] J. Wang, Y. Li, X. Sun, *Nano Energy* **2013**, *2*, 443.
[4] L. Dai, Y. Xue, L. Qu, H.-J. Choi, J.-B. Baek, *Chem. Rev.* **2015**, *115*, 4823.
[5] R. Paul, L. Zhu, H. Chen, J. Qu, L. Dai, *Adv. Mater.* **2019**, *31*, 1806403.
[6] K. Gong, F. Du, Z. Xia, M. Durstock, L. Dai, *Science* **2009**, *323*, 760.
[7] T. M. Gür, *Energy Environ. Sci.* **2018**, *11*, 2696.
[8] H. Zhao, Y. Lei, *Adv. Energy Mater.* **2020**, *10*, 2001460.
[9] Z. Xiang, Q. Dai, J. F. Chen, L. Dai, *Adv. Mater.* **2016**, *28*, 6253.
[10] I. Vlasov, O. I. Lebedev, V. G. Ralchenko, E. Goovaerts, G. Bertoni, G. Van Tendeloo, V. I. Konov, *Adv. Mater.* **2007**, *19*, 4058.
[11] Z. W. Seh, J. Kibsgaard, C. F. Dickens, I. Chorkendorff, J. K. Nørskov, T. F. Jaramillo, *Science* **2017**, *355*, aad4998.
[12] L. Zhao, Y. Guo, C. Fu, L. Luo, G. Wei, S. Shen, J. Zhang, *Chin. J. Catal.* **2021**, *42*, 2068.
[13] N. Daems, X. Sheng, I. F. J. Vankelecom, P. P. Pescarmona, *J. Mater. Chem. A* **2014**, *2*, 4085.
[14] X. Liu, L. Dai, *Nat. Rev. Mater.* **2016**, *1*, 16064.
[15] X. Zhang, T. Wang, L. Xiao, G. Xiang, W. Xu, Q. Huang, *Int. J. Hydrogen Energy* **2023**, *48*, 26979.
[16] Y.-M. Zhao, F.-F. Wang, P.-J. Wei, G.-Q. Yu, S.-C. Cui, J.-G. Liu, *ChemistrySelect* **2018**, *3*, 207.
[17] K. Iwase, T. Yoshioka, S. Nakanishi, K. Hashimoto, K. Kamiya, *Angew. Chem., Int. Ed.* **2015**, *54*, 11068.
[18] L. Gan, M. Wang, L. Hu, J. Fang, Y. Lai, J. Li, *ChemCatChem* **2018**, *10*, 1321.
[19] Z. Lu, J. Chen, W. Wang, W. Li, M. Sun, Y. Wang, X. Wang, J. Ye, H. Rao, *Small* **2021**, *17*, 2007326.
[20] J. Li, Y. Song, G. Zhang, H. Liu, Y. Wang, S. Sun, X. Guo, *Adv. Funct. Mater.* **2017**, *27*, 1604356.
[21] L. Liu, X. Rao, S. Zhang, J. Zhang, *Chem* **2024**, *10*, 1994.
[22] Z. Miao, X. Wang, Z. Zhao, W. Zuo, S. Chen, Z. Li, Y. He, J. Liang, F. Ma, H.-L. Wang, G. Lu, Y. Huang, G. Wu, Q. Li, *Adv. Mater.* **2021**, *33*, 2006613.
[23] K. P. Singh, E. J. Bae, J.-S. Yu, *J. Am. Chem. Soc.* **2015**, *137*, 3165.
[24] A. Kumar, J. M. Gonçalves, A. R. Lima, T. A. Matias, M. Nakamura, J. S. Bernardes, K. Araki, M. Bertotti, *Electrochim. Acta* **2019**, *326*, 134984.
[25] H. Xu, D. Wang, P. Yang, A. Liu, R. Li, Y. Li, L. Xiao, X. Ren, J. Zhang, M. An, *J. Mater. Chem. A* **2020**, *8*, 23187.
[26] J. Huang, Q. Lu, X. Ma, X. Yang, *J. Mater. Chem. A* **2018**, *6*, 18488.
[27] J. Tao, X. Wang, M. Xu, C. Liu, J. Ge, W. Xing, *Ind. Chem. Mater.* **2023**, *1*, 388.
[28] W. Wang, R. Wang, S. Ji, H. Feng, H. Wang, Z. Lei, *J. Power Sources* **2010**, *195*, 3498.
[29] J. Liu, Z. Liu, H. Wang, B. Liu, N. Zhao, C. Zhong, W. Hu, *Adv. Funct. Mater.* **2022**, *32*, 2110702.

© 2025 Wiley-VCH GmbH

16136829, 2026, 6, Downloaded from https://onlinelibrary.wiley.com/doi/10.1002/smll.202512014 by Jeonbuk National University, Wiley Online Library on [18/10/2026]. See the Terms and Conditions (https://onlinelibrary.wiley.com/terms-and-conditions) on Wiley Online Library for rules of use; OA articles are governed by the applicable Creative Commons License

[30] T. D. Le, D. Van Dao, G. Adilbish, Y.-T. Yu, *Int. J. Hydrogen Energy* **2022**, *47*, 1833.
[31] Y. Chen, Z. Jin, J. Sun, S. Chen, J. Zhang, S. Zhang, *eScience* **2025**, *5*, 100396.
[32] Y. Chen, L. Sun, Y. Jiao, J. Sun, Z. Jin, P. Li, S. Chen, S. Zhang, *Small* **2025**, *21*, 2500795.
[33] B. Qiao, A. Wang, X. Yang, L. F. Allard, Z. Jiang, Y. Cui, J. Liu, J. Li, T. Zhang, *Nat. Chem.* **2011**, *3*, 634.
[34] J. Yang, Y. Huang, H. Qi, C. Zeng, Q. Jiang, Y. Cui, Y. Su, X. Du, X. Pan, X. Liu, W. Li, B. Qiao, A. Wang, T. Zhang, *Nat. Commun.* **2022**, *13*, 4244.
[35] M. Li, K. Duanmu, C. Wan, T. Cheng, L. Zhang, S. Dai, W. Chen, Z. Zhao, P. Li, H. Fei, Y. Zhu, R. Yu, J. Luo, K. Zang, Z. Lin, M. Ding, J. Huang, H. Sun, J. Guo, X. Pan, W. A. Goddard, P. Sautet, Y. Huang, X. Duan, *Nat. Catal.* **2019**, *2*, 495.
[36] M. Liu, L. Wang, K. Zhao, S. Shi, Q. Shao, L. Zhang, X. Sun, Y. Zhao, J. Zhang, *Energy Environ. Sci.* **2019**, *12*, 2890.
[37] V. Dao, H. Choi, S. Yadav, J. D. Jiménez, C. Kim, T. Van Nguyen, K. Chen, P. Uthirakumar, Q. Van Le, S. D. Senanayake, H. Y. Kim, I.-H. Lee, *Appl. Catal. B Environ.* **2024**, *343*, 123452.
[38] V. H. Hoa, M. Austeria, H. T Dao, M. Mai, D. H. Kim, *Appl. Catal. B Environ.* **2023**, *327*, 122467.
[39] K. Liu, X. Zhao, G. Ren, T. Yang, Y. Ren, A. F. Lee, Y. Su, X. Pan, J. Zhang, Z. Chen, J. Yang, X. Liu, T. Zhou, W. Xi, J. Luo, C. Zeng, H. Matsumoto, W. Liu, Q. Jiang, K. Wilson, A. Wang, B. Qiao, W. Li, T. Zhang, *Nat. Commun.* **2020**, *11*, 1263.
[40] S. Lu, X. Li, G. Zhang, S. Wang, *Nat. Commun.* **2025**, *16*, 4346.
[41] H. Shin, W.-G. Jung, D.-H. Kim, J.-S. Jang, Y. H. Kim, W.-T. Koo, J. Bae, C. Park, S.-H. Cho, B. J. Kim, I.-D. Kim, *ACS Nano* **2020**, *14*, 11394.
[42] Y. Xu, W. Zheng, X. Liu, L. Zhang, L. Zheng, C. Yang, N. Pinna, J. Zhang, *Mater. Horiz.* **2020**, *7*, 1519.
[43] H. Xiang, W. Feng, Y. Chen, *Adv. Mater.* **2020**, *32*, 1905994.
[44] L. Liang, H. Jin, H. Zhou, B. Liu, C. Hu, D. Chen, Z. Wang, Z. Hu, Y. Zhao, H.-W. Li, D. He, S. Mu, *Nano Energy* **2021**, *88*, 106221.
[45] D. Liu, A. Barbar, T. Najam, M. S. Javed, J. Shen, P. Tsiakaras, X. Cai, *Appl. Catal. B Environ.* **2021**, *297*, 120389.
[46] C.-C. Hou, L. Zou, L. Sun, K. Zhang, Z. Liu, Y. Li, C. Li, R. Zou, J. Yu, Q. Xu, *Angew. Chem., Int. Ed.* **2020**, *59*, 7384.
[47] B. Bawab, S. M. Thalluri, E. Kolíbalová, R. Zazpe, L. Jelinek, J. Rodriguez-Pereira, J. M. Macak, *Chem. Eng. J.* **2024**, *482*, 148959.
[48] C. B. Thompson, Y. Lu, A. M. Karim, *Ind. Eng. Chem. Res.* **2021**, *60*, 15960.
[49] Z. Sun, W. Shi, L. R. Smith, N. F. Dummer, H. Qi, Z. Sun, G. J. Hutchings, *Nat. Commun.* **2025**, *16*, 3935.
[50] R. Chen, S. Chen, L. Wang, D. Wang, *Adv. Mater.* **2024**, *36*, 2304713.
[51] F. Xiao, Q. Wang, G.-L. Xu, X. Qin, I. Hwang, C.-J. Sun, M. Liu, W. Hua, H. Wu, S. Zhu, J.-C. Li, J.-G. Wang, Y. Zhu, D. Wu, Z. Wei, M. Gu, K. Amine, M. Shao, *Nat. Catal.* **2022**, *5*, 503.
[52] W. Luo, Y. Wang, L. Luo, S. Gong, M. Wei, Y. Li, X. Gan, Y. Zhao, Z. Zhu, Z. Li, *ACS Catal.* **2022**, *12*, 1167.
[53] Y. Ma, H. Fan, C. Wu, M. Zhang, J. Yu, L. Song, K. Li, J. He, *Carbon* **2021**, *185*, 526.
[54] X. Lin, L. Zeng, M. Wu, *J. Mater. Chem. A* **2024**, *12*, 17793.
[55] C. Liu, B. Qiao, T. Zhang, *JACS Au* **2024**, *4*, 4129.
[56] T. Rodenas, G. Prieto, *ChemCatChem* **2022**, *14*, 202201058.
[57] I. B. Aragão, F. R. Estrada, D. H. Barrett, C. B. Rodella, *Mol. Catal.* **2022**, *526*, 112377.
[58] M. Liu, J. Lee, T.-C. Yang, F. Zheng, J. Zhao, C.-M. Yang, L. Y. S. Lee, *Small Methods* **2021**, *5*, 2001165.
[59] H. Hu, Y. Meng, Y. Mei, P. Hou, C. Liu, H. Cheng, M. Shao, J. Li, *Energy Storage Mater.* **2023**, *54*, 517.
[60] J. Wu, J. Rong, C. Wang, C. Wang, N. Fang, Y. Zhang, H. Ao, C. Jing, Y. Yamauchi, Z. Zhou, Z. Li, *Chem. Eng. J.* **2025**, *511*, 162281.
[61] Y.-Y. Yang, L. He, P.-F. Xie, P. Dong, H. Quan, T. Li, L. Fang, D. Feng, Y. Xing, J.-C. Li, *Inorg. Chem. Front.* **2025**, *12*, 4409.
[62] W. Zhu, J. Fu, J. Liu, Y. Chen, X. Li, K. Huang, Y. Cai, Y. He, Y. Zhou, D. Su, J.-J. Zhu, Y. Lin, *Appl. Catal. B Environ.* **2020**, *264*, 118502.
[63] Y. Wang, D. Wang, Y. Li, *J. Energy Chem.* **2022**, *65*, 103.
[64] L. Wang, Y. Yang, Y. Shi, W. Liu, Z. Tian, X. Zhang, L. Zheng, S. Hong, M. Wei, *Chem Catal.* **2023**, *3*, 100483.
[65] X. Wan, Q. Liu, J. Liu, S. Liu, X. Liu, L. Zheng, J. Shang, R. Yu, J. Shui, *Nat. Commun.* **2022**, *13*, 2963.
[66] D. Zhang, Q. Zhang, C. Peng, Z. Long, G. Zhuang, D. Kramer, S. Komarneni, C. Zhi, D. Xue, *iScience* **2023**, *26*, 106624.
[67] B. Hammer, J. K. Norskov, *Nature* **1995**, *376*, 238.
[68] L. Yu, D. Deng, X. Bao, *Angew. Chem., Int. Ed.* **2020**, *59*, 15294.
[69] S. Jiao, X. Fu, H. Huang, *Adv. Funct. Mater.* **2022**, *32*, 2107651.
[70] L. Li, X. Wu, R. Zhang, N. Bai, M. Zhang, Y. Wen, *Sci. Rep.* **2025**, *15*, 8846.
[71] X. Wei, S. Song, W. Cai, Y. Kang, Q. Fang, L. Ling, Y. Zhao, Z. Wu, X. Song, X. Xu, S. M. Osman, W. Song, T. Asahi, Y. Yamauchi, C. Zhu, *ACS Nano* **2024**, *18*, 4308.
[72] J. Bai, Y. Fu, P. Zhou, P. Xu, L. Wang, J. Zhang, X. Jiang, Q. Zhou, Y. Deng, *ACS Appl. Mater. Interfaces* **2022**, *14*, 29986.
[73] Z. Mao, G. Wei, L. Liu, T. Hao, X. Wang, S. Tang, *J. Colloid Interface Sci.* **2025**, *679*, 860.
[74] Y. Zhang, Z. Wang, Y. Huo, X. Ju, K. Liu, W. Kang, P. Zhang, Z. Li, H. Li, *Chem. Eng. J.* **2025**, *524*, 169464.
[75] C. Yang, Y. Li, X. Wang, L. Zheng, H.-P. Liang, *ACS Appl. Nano Mater.* **2023**, *6*, 16016.
[76] Y. Pan, X. Ma, M. Wang, X. Yang, S. Liu, H.-C. Chen, Z. Zhuang, Y. Zhang, W.-C. Cheong, C. Zhang, X. Cao, R. Shen, Q. Xu, W. Zhu, Y. Liu, X. Wang, X. Zhang, W. Yan, J. Li, H. M. Chen, C. Chen, Y. Li, *Adv. Mater.* **2022**, *34*, 2203621.
[77] W. Zhou, H. Su, Z. Wang, F. Yu, W. Wang, X. Chen, Q. Liu, *J. Mater. Chem. A* **2021**, *9*, 1127.
[78] Z. Liu, S. Zhou, S. Ma, J. Li, Z. Yang, H. Cheng, W. Cai, *Mater. Today Phys.* **2021**, *17*, 100338.
[79] J. Hao, Z. Zhuang, J. Hao, C. Wang, S. Lu, F. Duan, F. Xu, M. Du, H. Zhu, *Adv. Energy Mater.* **2022**, *12*, 2200579.
[80] L. Chong, J. Wen, J. Kubal, F. G. Sen, J. Zou, J. Greeley, M. Chan, H. Barkholtz, W. Ding, D.-J. Liu, *Science* **2018**, *362*, 1276.
[81] Y. Zhang, D. Wang, G. Wei, B. Li, Z. Mao, S.-M. Xu, S. Tang, J. Jiang, Z. Li, X. Wang, X. Xu, *JACS Au* **2024**, *4*, 1509.
[82] T. D. Le, D.-S. Kim, T. Van Tran, B. Urupalli, G.-S. Shin, G.-J. Oh, Y.-T. Yu, *Small* **2024**, *20*, 2311971.
[83] N. A. Ishiki, K. Teixeira Santos, N. Bibent, K. Kumar, I. Reichmann, Y.-P. Ku, T. Asset, L. Dubau, M. Mermoux, H. Ge, S. Berthon-Fabry, V. A. Saveleva, V. K. Paidi, P. Glatzel, A. Zitolo, T. Mineva, H. Guesmi, S. Cherevko, E. A. Ticianelli, F. Maillard, F. Jaouen, *Nat. Commun.* **2025**, *16*, 6404.
[84] Y. Sun, J. Luo, M. Zhang, J. Li, J. Yu, S. Lu, W. Song, Y. Wei, Z. Li, J. Liu, *ACS Appl. Mater. Interfaces* **2023**, *15*, 10696.
[85] P. Su, W. Pei, X. Wang, Y. Ma, Q. Jiang, J. Liang, S. Zhou, J. Zhao, J. Liu, G. Q. (Max) Lu, *Angew. Chem., Int. Ed.* **2021**, *60*, 16044.
[86] Y. Sun, X. Leng, X. Jin, F. Chen, L. Huang, J. Yang, H. Zhang, H. Duan, B. Cao, *Appl. Surf. Sci.* **2025**, *710*, 163941.
[87] X. Lu, Y. Li, D. Dong, Y. Wan, R. Li, L. Xiao, D. Wang, L. Liu, G. Wang, J. Zhang, M. An, P. Yang, *J. Colloid Interface Sci.* **2024**, *653*, 654.
[88] X. Q. Mu, S. L. Liu, M. Y. Zhang, Z. C. Zhuang, D. Chen, Y. R. Liao, H. Y. Zhao, S. C. Mu, D. S. Wang, Z. H. Dai, *Angew. Chem., Int. Ed.* **2024**, *63*, 202319618.
[89] B. Sun, H. Lv, Q. Xu, P. Tong, P. Qiao, H. Tian, H. Xia, *Small* **2024**, *20*, 2400240.
[90] Y. Yang, Y. Xiao, L. Zhang, H.-T. Wang, K.-H. Chen, W.-X. Lin, N. Jin, C. Sun, Y.-C. Shao, J.-L. Chen, J. Qian, L. Han, *Appl. Catal. B Environ. Energy* **2024**, *347*, 123792.

© 2025 Wiley-VCH GmbH

16136829, 2026, 6, Downloaded from https://onlinelibrary.wiley.com/doi/10.1002/smll.202512014 by Jeonbuk National University, Wiley Online Library on [18/10/2026]. See the Terms and Conditions (https://onlinelibrary.wiley.com/terms-and-conditions) on Wiley Online Library for rules of use; OA articles are governed by the applicable Creative Commons License

[91] L. Zhuang, Z. Jia, Y. Wang, X. Zhang, S. Wang, J. Song, L. Tian, T. Qi, *Chem. Eng. J.* **2022**, *438*, 135585.
[92] Q. Wang, J. Zhao, R. Yu, D. Shen, C. Wu, K. H. Luo, L.-H. Xu, *J. Energy Inst.* **2023**, *111*, 101444.
[93] H. Liu, X. Xu, H. Xu, S. Wang, Z. Niu, Q. Jia, L. Yang, R. Cao, L. Zheng, D. Cao, *Appl. Catal. B Environ.* **2021**, *297*, 120451.
[94] X. Lu, C. Guo, M. Zhang, L. Leng, J. H. Horton, W. Wu, Z. Li, *Nano Res.* **2021**, *14*, 4347.
[95] S. Che, N. Ta, F. Yang, X. Yan, H. Liu, N. Chen, S. Sun, C. Wang, B. Jiang, Y. Sun, Y. Wang, Y. Li, *Mater. Chem. Front.* **2022**, *6*, 3577.
[96] Y. Wu, X. Tang, F. Zhang, L. Li, W. Zhai, B. Huang, T. Hu, D. Lützenkirchen-Hecht, K. Yuan, Y. Chen, *Mater. Chem. Front.* **2022**, *6*, 1209.
[97] J.-C. Li, Y. Meng, L. Zhang, G. Li, Z. Shi, P.-X. Hou, C. Liu, H.-M. Cheng, M. Shao, *Adv. Funct. Mater.* **2021**, *31*, 2103360.
[98] D. Cao, J. Wang, H. Xu, D. Cheng, *Small* **2021**, *17*, 2101163.
[99] Y. Zhang, P. Li, C. Zhao, G. Zhou, F. Zhou, Q. Zhang, C. Su, Y. Wu, *Sci. Bull.* **2022**, *67*, 1679.
[100] I. Poudyal, N. P. Adhikari, *J. Mol. Liq.* **2014**, *194*, 77.
[101] C. Hou, S. Gheorghiu, V. H. Huxley, P. Pfeifer, *PLoS Comput. Biol.* **2010**, *6*, 1000902.
[102] D. Chen, L.-H. Zhang, J. Du, H. Wang, J. Guo, J. Zhan, F. Li, F. Yu, *Angew. Chem., Int. Ed.* **2021**, *60*, 24022.
[103] Z. Yihui, T. Pengfei, J. Hongliang, M. Jingren, M. Lu, S. Xiaozhi, W. Yu, L. Yunxiang, Z. Yihua, S. Li, L. Chunzhong, *CCS Chem.* **2020**, *3*, 2539.
[104] W. Guo, X. Gao, M. Zhu, C. Xu, X. Zhu, X. Zhao, R. Sun, Z. Xue, J. Song, L. Tian, J. Xu, W. Chen, Y. Lin, Y. Li, H. Zhou, Y. Wu, *Energy Environ. Sci.* **2023**, *16*, 148.
[105] J. Lai, S. Chen, X. Liu, X. Yan, Z. Qin, L. Xie, Z. Lin, Z. Cai, Y. Zhao, H.-L. Wang, Y. Huang, Q. Li, *ACS Catal.* **2023**, *13*, 11996.
[106] L. Liu, A. Corma, *Chem. Rev.* **2018**, *118*, 4981.
[107] A. Corma, P. Concepción, M. Boronat, M. J. Sabater, J. Navas, M. J. Yacaman, E. Larios, A. Posadas, M. A. López-Quintela, D. Buceta, E. Mendoza, G. Guilera, A. Mayoral, *Nat. Chem.* **2013**, *5*, 775.
[108] P. Liu, Y. Zhao, R. Qin, S. Mo, G. Chen, L. Gu, D. M. Chevrier, P. Zhang, Q. Guo, D. Zang, B. Wu, G. Fu, N. Zheng, *Science* **2016**, *352*, 797.
[109] X. Rao, S. Zhang, J. Zhang, *Electrochem. Energy Rev.* **2025**, *8*, 7.
[110] H. Lee, H. Choi, J. Hwang, H. Kim, *ACS Sustainable Chem. Eng.* **2022**, *10*, 6181.
[111] Y. Mo, S. Feng, T. Yu, J. Chen, G. Qian, L. Luo, S. Yin, *J. Colloid Interface Sci.* **2022**, *607*, 1928.
[112] L. Huang, W. Li, M. Zeng, G. He, P. R. Shearing, I. P. Parkin, D. J. L. Brett, *Compos. Part B Eng.* **2021**, *220*, 108986.
[113] C. Xu, A. Vasileff, D. Wang, B. Jin, Y. Zheng, S.-Z. Qiao, *Nanoscale Horiz.* **2019**, *4*, 1411.
[114] A. Bagger, W. Ju, A. S. Varela, P. Strasser, J. Rossmeisl, *Catal. Today* **2017**, *288*, 74.
[115] T. Duc Le, M. J. Ahemad, D.-S. Kim, B.-H. Lee, G.-J. Oh, G.-S. Shin, L. R. Nagappagari, V. Dao, T. Van Tran, Y.-T. Yu, *J. Colloid Interface Sci.* **2023**, *634*, 930.
[116] J. N. Tiwari, S. Sultan, C. W. Myung, T. Yoon, N. Li, M. Ha, A. M. Harzandi, H. J. Park, D. Y. Kim, S. S. Chandrasekaran, W. G. Lee, V. Vij, H. Kang, T. J. Shin, H. S. Shin, G. Lee, Z. Lee, K. S. Kim, *Nat. Energy* **2018**, *3*, 773.
[117] J. Liu, J. Bak, J. Roh, K.-S. Lee, A. Cho, J. W. Han, E. Cho, *ACS Catal.* **2021**, *11*, 466.
[118] T. Luo, J. Huang, Y. Hu, C. Yuan, J. Chen, L. Cao, K. Kajiyoshi, Y. Liu, Y. Zhao, Z. Li, Y. Feng, *Adv. Funct. Mater.* **2023**, *33*, 2213058.
[119] C. Zhao, X. Dai, T. Yao, W. Chen, X. Wang, J. Wang, J. Yang, S. Wei, Y. Wu, Y. Li, *J. Am. Chem. Soc.* **2017**, *139*, 8078.
[120] V. Armel, S. Hindocha, F. Salles, S. Bennett, D. Jones, F. Jaouen, *J. Am. Chem. Soc.* **2017**, *139*, 453.
[121] Y. Cheng, S. He, S. Lu, J.-P. Veder, B. Johannessen, L. Thomsen, M. Saunders, T. Becker, R. De Marco, Q. Li, S. Yang, S. P. Jiang, *Adv. Sci.* **2019**, *6*, 1802066.
[122] P. Guo, H. Li, B. Huang, D. Ji, G. Li, X. Zhao, *Langmuir* **2025**, *41*, 23582.
[123] F. Zheng, Y. Yang, Q. Chen, *Nat. Commun.* **2014**, *5*, 5261.
[124] W. Zhang, H. Li, D. Feng, C. Wu, C. Sun, B. Jia, X. Liu, T. Ma, *Carbon Energy* **2024**, *6*, 461.
[125] L. Yang, G. Xu, J. Ban, L. Zhang, G. Xu, Y. Lv, D. Jia, *J. Colloid Interface Sci.* **2019**, *535*, 415.
[126] X. Ao, W. Zhang, B. Zhao, Y. Ding, G. Nam, L. Soule, A. Abdelhafiz, C. Wang, M. Liu, *Energy Environ. Sci.* **2020**, *13*, 3032.
[127] M. Wu, X. Yang, X. Cui, N. Chen, L. Du, M. Cherif, F.-K. Chiang, Y. Wen, A. Hassanpour, F. Vidal, S. Omanovic, Y. Yang, S. Sun, G. Zhang, *Nano-Micro Lett.* **2023**, *15*, 232.
[128] S. Yang, C. Wu, J. Wang, H. Shen, K. Zhu, X. Zhang, Y. Cao, Q. Zhang, H. Zhang, *ACS Catal.* **2022**, *12*, 971.
[129] J. Chen, B. Huang, R. Cao, L. Li, X. Tang, B. Wu, Y. Wu, T. Hu, K. Yuan, Y. Chen, *Adv. Funct. Mater.* **2023**, *33*, 2209315.
[130] F. Zhou, Y. Ruan, M. Zhu, X. Gao, W. Guo, X. Liu, W. Wang, M. Chen, G. Wu, T. Yao, H. Zhou, Y. Wu, *Small* **2023**, *19*, 2302328.
[131] S. Wei, A. Li, J.-C. Liu, Z. Li, W. Chen, Y. Gong, Q. Zhang, W.-C. Cheong, Y. Wang, L. Zheng, H. Xiao, C. Chen, D. Wang, Q. Peng, L. Gu, X. Han, J. Li, Y. Li, *Nat. Nanotechnol.* **2018**, *13*, 856.
[132] T. D. Le, D.-S. Kim, G.-J. Oh, G.-S. Shin, T. Van Tran, B.-G. Ahn, Y.-T. Yu, *Sustain. Mater. Technol.* **2024**, *41*, 01068.
[133] T.-H. Le, H. Yoon, *Carbon* **2019**, *152*, 796.
[134] V. Pavlenko, S. Khosravi H, S. Żółtowska, A. B. Haruna, M. Zahid, Z. Mansurov, Z. Supiyeva, A. Galal, K. I. Ozoemena, Q. Abbas, T. Jesionowski, *Mater. Sci. Eng. R Rep.* **2022**, *149*, 100682.
[135] N. Díez, M. Sevilla, A. B. Fuertes, *Carbon* **2021**, *178*, 451.
[136] A. Eftekhari, Z. Fan, *Mater. Chem. Front.* **2017**, *1*, 1001.
[137] J. Melke, R. Schuster, S. Möbus, T. Jurzinsky, P. Elsässer, A. Heilemann, A. Fischer, *Carbon* **2019**, *146*, 44.
[138] Z. Zeng, S. Küspert, S. E. Balaghi, H. E. M. Hussein, N. Ortlieb, M. Knäbbeler-Buß, P. Hügenell, S. Pollitt, N. Hug, J. Melke, A. Fischer, *Small* **2023**, *19*, 2205885.

© 2025 Wiley-VCH GmbH

16136829, 2026, 6, Downloaded from https://onlinelibrary.wiley.com/doi/10.1002/smll.202512014 by Jeonbuk National University, Wiley Online Library on [18/10/2026]. See the Terms and Conditions (https://onlinelibrary.wiley.com/terms-and-conditions) on Wiley Online Library for rules of use; OA articles are governed by the applicable Creative Commons License



Thanh Duc Le is currently Lecturer and Researcher at Institute for Research and Development, Duy Tan University. He obtained his Ph.D. in Material Science from Jeonbuk National University in 2024 and conducted his postdoctoral training at University of Freiburg, Germany. His research interests focus on developing advanced materials for energy conversion and storage.



Van Hien Hoa Van Hien Hoa received his engineering degree in Materials Science and Engineering from Hanoi University of Science and Technology, Vietnam. In August 2021, he obtained his Ph.D. from the Department of Nano Convergence Engineering at Jeonbuk National University, Korea. His research focuses on the synthesis and application of nanomaterials for energy conversion, particularly the development of catalyst materials for electrochemical hydrogen production from water and seawater splitting, as well as for fuel cells and batteries.



Khoa Dang Tran obtained his Ph.D. in Nano Convergence Engineering from Jeonbuk National University, South Korea, in 2025. He is currently a lecturer at the University of Transport Technology, Vietnam. His research interest is the design of novel nanomaterials for water splitting, metal-air batteries, and gas sensing applications.



Do Hwan Kim received his Ph.D. degrees in Chemistry from Korea Advanced Institute of Science and Technology (KAIST) in 2005. Then he became a professor at Chemistry Education, Daegu University, and moved to Jeonbuk National University in 2015. His research topic was the organic functionalization of semiconductor surface. His current research centers on theoretical study of new-generation nanomaterials for energy conversion/storage applications.

© 2025 Wiley-VCH GmbH

16136829, 2026, 6, Downloaded from https://onlinelibrary.wiley.com/doi/10.1002/smll.202512014 by Jeonbuk National University, Wiley Online Library on [18/10/2026]. See the Terms and Conditions (https://onlinelibrary.wiley.com/terms-and-conditions) on Wiley Online Library for rules of use; OA articles are governed by the applicable Creative Commons License



Vandung Dao received his Ph.D. degree in Advanced Materials Engineering from Jeonbuk National University, South Korea (2019). He is currently serving as a Research Professor at Korea University, South Korea, and is focusing on the synthesis of alloys, metal/semiconductors hybrid and core@shell nanostructures for advanced catalysis applications such as water splitting for hydrogen and oxygen evolution, CO_2 reduction reactions, and chemical gas sensors.



In-Hwan Lee received his Ph.D. degree in materials science and engineering from Korea University, Korea in 1997. During 1997–1999, he was a postdoctoral fellow at Northwestern University. From 2002–2017, he was a faculty member at School of Advanced Materials Engineering, Jeonbuk National University, Korea. With the sabbatical grant from LG foundation, he was at Yale University during 2008–2009. In 2017, he joined Department of Materials Engineering, Korea University, Korea as a full professor. His current research focuses on the development of nanotechnology-inspired novel optoelectronic devices including micro/nano LEDs, photovoltaic devices, sensors, and photocatalysts.



Dong-Seog Kim is currently a Ph.D. candidate at the Division of Advanced Materials Engineering, Jeonbuk National University. He obtained his master's degree (MS) in 2022 from Jeonbuk National University. His research interests include metal-alloy catalysts and various nanostructure materials such as the core-shell nanoparticles for chemical gas sensors and photocatalyst applications.



Tuong Van Tran received his Ph.D. degree in 2025 from Jeonbuk National University, South Korea. He is currently serving as a Postdoctoral Researcher at the Division of Advanced Materials Engineering, Jeonbuk National University. His research interests are in the synthesis of metal@oxide core-shell nanoparticles and their application for gas sensors.

© 2025 Wiley-VCH GmbH

16136829, 2026, 6, Downloaded from https://onlinelibrary.wiley.com/doi/10.1002/smll.202512014 by Jeonbuk National University, Wiley Online Library on [18/10/2026]. See the Terms and Conditions (https://onlinelibrary.wiley.com/terms-and-conditions) on Wiley Online Library for rules of use; OA articles are governed by the applicable Creative Commons License



Yeon-Tae Yu is a professor in the Division of Advanced Materials Engineering at Jeonbuk National University, South Korea. He received his B.S. and M.S. degrees from Jeonbuk National University in 1986 and 1988, respectively, and received Doctoral degree in 1993 from Tohoku University, Japan. From 1993 to 2003, he was a Senior Researcher at Korea Institute of Geoscience and Mineral Resources (KIGAM). In 2004, he moved to Division of Advanced Materials Engineering of Jeonbuk National University as assistant professor. His current research interests are synthesis of core-shell structure composite nanoparticles and their applications for photocatalysts, gas sensors and fuel cells.

© 2025 Wiley-VCH GmbH

16136829, 2026, 6, Downloaded from https://onlinelibrary.wiley.com/doi/10.1002/smll.202512014 by Jeonbuk National University, Wiley Online Library on [18/10/2026]. See the Terms and Conditions (https://onlinelibrary.wiley.com/terms-and-conditions) on Wiley Online Library for rules of use; OA articles are governed by the applicable Creative Commons License